2023-06

AN IMPACT TO US NAVAL OPERATIONS: PREDICTING JELLYFISH BLOOMS IN THE ARABIAN SEA

Geant, Stephanie A.

Monterey, CA; Naval Postgraduate School

NAVAL POSTGRADUATE SCHOOL

MONTEREY, CALIFORNIA

THESIS

**AN IMPACT TO U.S. NAVAL OPERATIONS:
PREDICTING JELLYFISH BLOOMS
IN THE ARABIAN SEA**

by

Stephanie A. Geant

June 2023

Thesis Advisor: Tetyana Margolina
Second Reader: John E. Joseph

THIS PAGE INTENTIONALLY LEFT BLANK

REPORT DOCUMENTATION PAGE	*Form Approved OMB No. 0704-0188*

1. AGENCY USE ONLY *(Leave blank)*	**2. REPORT DATE** June 2023	**3. REPORT TYPE AND DATES COVERED** Master's thesis

4. TITLE AND SUBTITLE AN IMPACT TO U.S. NAVAL OPERATIONS: PREDICTING JELLYFISH BLOOMS IN THE ARABIAN SEA	**5. FUNDING NUMBERS**
6. AUTHOR(S) Stephanie A. Geant	
7. PERFORMING ORGANIZATION NAME(S) AND ADDRESS(ES) Naval Postgraduate School Monterey, CA 93943-5000	**8. PERFORMING ORGANIZATION REPORT NUMBER**
9. SPONSORING / MONITORING AGENCY NAME(S) AND ADDRESS(ES) N/A	**10. SPONSORING / MONITORING AGENCY REPORT NUMBER**

11. SUPPLEMENTARY NOTES The views expressed in this thesis are those of the author and do not reflect the official policy or position of the Department of Defense or the U.S. Government.

12a. DISTRIBUTION / AVAILABILITY STATEMENT Approved for public release. Distribution is unlimited.	**12b. DISTRIBUTION CODE** A

13. ABSTRACT (maximum 200 words)

Operations of two U.S. Navy aircraft carriers in the Arabian Sea were inhibited by the *Crambionella orsini* (*c. orsini*) jellyfish bloom in 2020, causing degradation to their propulsion systems. *C. orsini* bloom also occurred in 2002, but did not impact naval operations. We compared the two bloom years by calculating Ekman transport to characterize upwelling, using Empirical Orthogonal Function analysis to detect oceanic variability patterns, and analyzing temperature, chlorophyll-a, and mixed layer depth as potential bloom predictors. This research found no single cause but a combination of environmental conditions, which include upwelling-favorable monsoonal winds and moderate sea surface temperature (SST). Upwelled nutrient-rich waters cause increased primary productivity of mixed diatoms eaten by dinoflagellates, a food source for *C. orsini*. The jellyfish and their food source are advected to moderate temperature regions by the monsoonal circulation. It was shown that when SST is below 25°C or above 30°C, *c. orsini* cease blooming as their food source diminishes. To forecast a bloom, *c. orsini* must be present in coastal waters with an overabundance of nutrients during either monsoon season. The main environmental driver of a *c. orsini* bloom is the monsoon season, and the limiting factor is the SST. The blooms, although rare, can jeopardize our effectiveness to prevail in day-to-day competition; understanding these blooms allows warfighters to maintain the Navy's advantage at sea.

14. SUBJECT TERMS sea surface temperature, jellyfish bloom, upwelling, monsoon, interannual variability, fleet readiness, tactical decision aid, oceanography, Ekman transport	**15. NUMBER OF PAGES** 77
	16. PRICE CODE

17. SECURITY CLASSIFICATION OF REPORT Unclassified	**18. SECURITY CLASSIFICATION OF THIS PAGE** Unclassified	**19. SECURITY CLASSIFICATION OF ABSTRACT** Unclassified	**20. LIMITATION OF ABSTRACT** UU

NSN 7540-01-280-5500

Standard Form 298 (Rev. 2-89)
Prescribed by ANSI Std. 239-18

THIS PAGE INTENTIONALLY LEFT BLANK

Approved for public release. Distribution is unlimited.

AN IMPACT TO U.S. NAVAL OPERATIONS: PREDICTING JELLYFISH BLOOMS IN THE ARABIAN SEA

Stephanie A. Geant
Lieutenant Commander, United States Navy
BS, United States Naval Academy, 2012
MA, University of Oklahoma, 2018

Submitted in partial fulfillment of the
requirements for the degree of

MASTER OF SCIENCE IN METEOROLOGY AND PHYSICAL OCEANOGRAPHY

from the

NAVAL POSTGRADUATE SCHOOL
June 2023

Approved by: Tetyana Margolina
Advisor

John E. Joseph
Second Reader

Peter C. Chu
Chair, Department of Oceanography

THIS PAGE INTENTIONALLY LEFT BLANK

ABSTRACT

Operations of two U.S. Navy aircraft carriers in the Arabian Sea were inhibited by the *Crambionella orsini* (*c. orsini*) jellyfish bloom in 2020, causing degradation to their propulsion systems. *C. orsini* bloom also occurred in 2002 but did not impact naval operations. We compared the two bloom years by calculating Ekman transport to characterize upwelling using Empirical Orthogonal Function analysis to detect oceanic variability patterns and analyzing temperature, chlorophyll-a, and mixed layer depth as potential bloom predictors. This research found no single cause but a combination of environmental conditions, which include upwelling-favorable monsoonal winds and moderate sea surface temperature (SST). Upwelled nutrient-rich waters cause increased primary productivity of mixed diatoms eaten by dinoflagellates, a food source for *C. orsini*. The jellyfish and their food source are advected to moderate temperature regions by the monsoonal circulation. It was shown that when SST is below 25°C or above 30°C, *c. orsini* cease blooming as their food source diminishes. To forecast a bloom, *c. orsini* must be present in coastal waters with an overabundance of nutrients during either monsoon season. The main environmental driver of a *c. orsini* bloom is the monsoon season, and the limiting factor is the SST. The blooms although rare can jeopardize our effectiveness to prevail in day-to-day competition; understanding these blooms allows warfighters to maintain the Navy's advantage at sea.

THIS PAGE INTENTIONALLY LEFT BLANK

TABLE OF CONTENTS

LIST OF FIGURES

LIST OF TABLES

THIS PAGE INTENTIONALLY LEFT BLANK

LIST OF ACRONYMS AND ABBREVIATIONS

3D-VAR	three-dimensional variational assimilation
AS	Arabian Sea
AVHRR	Advanced Very High-Resolution Radiometer
ASCAT-A	Advanced Scatterometer
c. orsini	*Crambionella orsini*
CHL-A	chlorophyll-a
CORA	CMEMS Coriolis Ocean Dataset for Reanalysis
CFSR	Climate Forecasting System Reanalysis
CMEMS	Copernicus Marine Environment Monitoring Service
DMI	Dipole Mode Index
ECMWF-ERA	European Centre for Medium Range Weather forecast reanalysis
ENSO	El Nino Southern Oscillation
EOF	Empirical Orthogonal Function, eigenmodes
ET	Ekman transport
ETRS89	European Terrestrial Reference System 1989
GEBCO	General Bathymetric Chart of the Ocean
GOO	Gulf of Oman
HY-2B	Hai Yang 2B
HYCOM	Hybrid Coordinate Ocean Model
IOD	Indian Ocean Dipole
MLD	mixed layer depth
n. scintillians	*Noctiluca scintillans*
PLA Navy	People's Liberation Army Navy
PC	principal components

SEEK	Singular Evolutive Extended Kalman
SCATSAT	Scatterometer Satellite
SLA	sea level anomaly
SSMIS	Special Sensor Microwave Imager Sounder
SSH	sea surface height
SST	sea surface temperature
TDA	tactical decision aid
TEMP	temperature
T/S	temperature/salinity
U.S.	United States
WGS	World Geodetic System
z	depth

ACKNOWLEDGMENTS

This research would not have been possible without the help of my thesis advisor, Dr. Tetyana Margolina. Her expertise, dedication, and mentorship were unwavering, thank you is an understatement! Thank you also to the oceanography department, especially Mike Cook and CDR John Joseph, USN (ret), for providing me with the foundation and MATLAB tools to write my thesis. Lastly, I am grateful to my husband, Rob, and sons for welcoming and supporting my jellyfish obsession these past few years. I greatly appreciate you all!

THIS PAGE INTENTIONALLY LEFT BLANK

I. INTRODUCTION

A. WHAT IS THE THREAT OF JELLYFISH TO U.S. NAVAL OPERATIONS?

Jellyfish have existed for over 400 million years (Pitt and Lucas, 2014) and the modern-day U. S. Navy has executed operations for over a century. However, in recent years jellyfish blooms are jeopardizing our Navy's advantage at sea by impacting naval operations. Jellyfish are "blooming" when rapid onset of the species occurs at a particular time and place in highly elevated concentrations (Pitt and Lucas, 2014). Jellyfish have curtailed ships' maneuverability, flight operations, and our overall effectiveness to prevail in day-to-day competition. Significant jellyfish blooms, such as the occurrence of the *Crambionella Orsini (c. orsini)* bloom in the Arabian Sea (AS) in 2020, have affected operations of two different U.S. Navy aircraft carriers. On record, a similar *c. orsini* bloom also occurred in 2002 but did not affect naval operations. Degradation to an aircraft carrier's propulsion systems caused by the bloom prevents naval operations from continuing. Furthermore, the Mediterranean Sea and Coral Sea also had blooms that restricted U.S. aircraft carrier operations. With the current military focus on the Western Pacific, there is justification in focusing on the increasing jellyfish blooms in the Yellow Sea, Bohai Sea, and northern East China Sea (Dong et al. 2010). Additionally, this increased jellyfish production in the coastal and offshore regions has resulted in the People's Liberation Army Navy (PLA Navy) taking a proactive stance in developing a jellyfish shredder to prevent whole-bodied jellyfish from entering their ship's engine intakes (Mizokami 2017). The U.S. Navy currently lacks the ability to predict when a jellyfish bloom will occur. With a small record of bloom occurrence, it would be beneficial to understand the conditions for when a bloom does not occur. With over 1200 different species of jellyfish (Pitt and Lucas 2014) present worldwide, determining the oceanographic and climatological parameters specific to the bloom-forming species is crucial to ensuring the U.S. Navy can continue to operate in contested waters and utilize the bloom occurrence to our advantage.

The objective of this thesis is to determine the main environmental drivers and limiting factors of the endemic *c. orsini* blooms in the AS and Gulf of Oman (GOO) and to facilitate forecasts with a 1–2 day lead time by using easy-to-interpret oceanographic information. Future work includes development of a tactical decision aid (TDA) which would identify areas of predicted and active blooms. Currently, a scientific cause of the *c. orsini* is still unknown and no consensus exists among the scientific community about the predictability of these events. This deficiency is due to aperiodicity, diversity and multi-scale nature of jellyfish blooms, lack of long-term records on their occurrences and understanding of the interplay of biological/oceanographic bloom-favorable conditions.

B. GLOBAL CHANGES

Since the 1970s, there has been a notable increase in jellyfish blooms worldwide with a distinguishable decadal oscillation (Pitt and Lucas 2014). Global changes attributed to this increase include climate and habitat change, eutrophication, and overfishing (Purcell et al. 2007). With over a thousand different types of jellyfish, many bloom increases are multifaceted and affected by a combination of factors that occur at different time scales.

Data from climate change studies suggest global temperatures are expected to increase .1-.2°C per decade (Purcell et al. 2007). Warmer air temperatures correlate to an increase in ocean temperatures. With this temperature increase, jellyfish reproduction also increases (Lamb 2017). Jellyfish's habitat change is rapidly occurring to accommodate the 18% growth by 2050 of the human population (U.S. Census Bureau 2011). As more coastal construction occurs to house the growing human population, there are more surfaces for polyps to grow on, which is a jellyfish food source (Purcell et al. 2007). As dams are constructed, the maritime waters are altered affecting the ecosystem in this area. The creation of nuclear and thermal power plants requires seawater cooling and discharges warm water back into the ocean environment (Purcell et al. 2007). This discharge provides the perfect habitat for jellyfish blooms to occur (Purcell et al. 2007).

In coastal waters, eutrophication is a major global pollution problem as land run off affects the chemical balance of the ocean. The increased nutrients and concentration changes result in overproduction of jellyfish food such as phytoplankton and zooplankton.

Overproduction of food enhances the feeding and growth of the jellyfish (Purcell et al. 2007). Additionally, eutrophication affects water clarity and light penetration (Purcell et al. 2007). With reduced sunlight, it is more difficult for fish and other visual feeders to find their prey (Purcell et al. 2007). Thus, leaving more food available for jellyfish, who are non-visual feeders (Purcell et al. 2007). Overfishing positively increases the jellyfish population as competitors that feed off jellyfish are removed from the food chain (Pitt and Lucas 2014). Without the larger prey to eat the jellyfish, more jellyfish equate to more jellyfish being able to reproduce, continuing the positive feedback loop. In summary, climate and habitat change, eutrophication, and overfishing, are not mutually exclusive of each other. Increases in various jellyfish species can be attributed to multiple interacting factors and vary globally. Overall, jellyfish are an adaptable species, demonstrated by their existence for millions of years.

C. COUNTERARGUMENT

A majority of scientific research papers, more than 85%, support that jellyfish and jellyfish blooms are increasing worldwide due to anthropogenic stressors or activity (Sanz-Martin et al. 2016). There is no scientific research supporting the contrary (Pitt et al. 2018). However, the research papers which support this increase are amplified beyond what evidence provides. Each of these aforementioned research papers reference one another further perpetuating this idea of jellyfish blooms increasing worldwide. Similarly, problematic blooms such as those in heavily, populated coastal regions garner a significant amount of media attention. These problematic blooms are a small fraction of the blooms that occur but persuade the population into thinking that jellyfish blooms must be increasing in occurrence. Public perception is based on current activity (Condon et al. 2013). Overall, stating that blooms are increasing because of these stressors is an exaggeration beyond what evidence provides (Pitt et al. 2018).

Furthermore, the perception of jellyfish blooms increasing can be described as part of the oscillation in its regular occurrence, with the current global state in the maximum of the oscillation (Pitt and Lucas 2014). There is a lack of historical data on jellyfish blooms and the perceived increase of jellyfish blooms could be caused by a shift in baselines

(Condon et al. 2013). Additionally, present-day jellyfish blooms coincide with the natural fluctuations in the environment. While a slight upward trend in occurrences is present when compared to the limited historical data; the upward trend is still within the normal range (Lamb 2017). Regardless of whether blooms are increasing, they have become a hinderance to conducting U.S. naval operations in the AS and GOO. Addressing the monsoonal environment, changes in global weather patterns, and their influence on marine plankton is the key to substantiating why *c. orsini* are more abundant in the region.

D. ARABIAN SEA AND GULF OF OMAN

The *c. orsini* jellyfish, common name doll jellyfish, are native to the western Indian Ocean from the Arabian Gulf to south of the Cape of Good Hope, originate in coastal waters, and were first discovered over 120 years ago (World Register of Marine Species 1997). The *c. orsini* bell width can be up to 20cm with varying color from brown to yellowish-brown (World Register of Marine Species 1997) (see Figure 1).

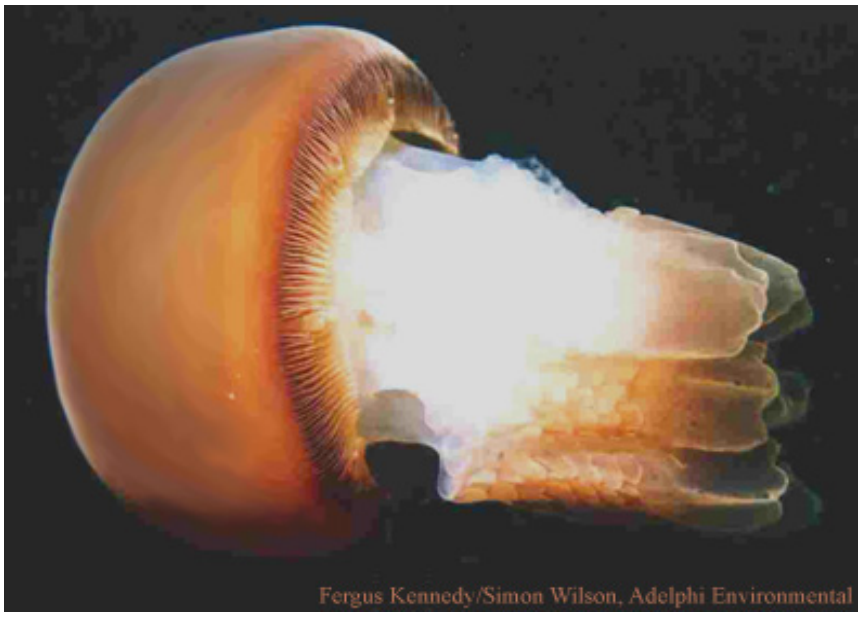

Figure 1. Photo of a *c. orsini* jellyfish. Source: Kennedy and Wilson (2013)

The *c. orsini* swim faster during daylight conditions, respond better to live feeds, and exhibit increased activity with increasing light intensities. (Soumya et al. 2021). The

activity and feeding habits are mentioned to make the connection with the *Noctiluca scintillans* (*n. scintillans)* a type of dinoflagellate or marine plankton, that are becoming overabundant in the region. The *n. scintillans,* nicknamed sea sparkles, bloom in the mid-late phase of the summer monsoon causing a red tide in the southeastern AS and bloom in the later phase of the winter monsoon causing a green tide in the northeastern AS (Thomas et al. 2020). The *c. orsini* are frequent feeders of the *n. scintillans,* which are undergoing a population explosion due to climate, habitat change, and eutrophication (Thomas et al. 2020). Upwelling along the southeastern AS in the summer and winter mixing along the northeastern AS cause nutrient availability in the water column to increase (Thomas et al. 2020). These mixed diatom blooms are eaten by the *n. scintillans* which, in turn, are eaten by the *c. orsini*.

Furthermore, measuring of chlorophyll in the surface water is an indication of nutrient availability. When nutrients availability increases then chlorophyll production increases. In the winter and summer months, the AS experiences sea surface temperature (SST) cooling thus increasing the nutrients in the water column. The ocean mechanisms causing the cooling in the summer months include upwelling and advection whereas the winter months experience convective mixing and reduced solar heating (Saxena and Menezes 2006). This seasonal increased nutrient availability correlates to the production of the mixed diatom blooms. Monitoring the remotely-sensed chlorophyll in the AS could be another indication of a potential *c. orsini* bloom. However, the interrelationship from upwelling to the abundant *c. orsini* blooms is not solely based on the outburst of *n. scintillans* but rather it is one factor contributing to habitat change in the region.

As mentioned earlier, the monsoon wind regime in the AS is very influential in driving the biological activity during the southwest and northeast monsoon. The southwest/ summer monsoon season is from June to September and the northeast/winter monsoon season is from December-February (Wiggert et al. 2005). Figure 2 describes the wind and current regime during the monsoon seasons. The southwest monsoon is characterized by ocean heat gain and upwelling in the GOO (Pourjomeh et al. 2017). The northeast monsoon is characterized by ocean heat loss and the convective overturning of the mixed layer (Pourjomeh et al. 2017). Both monsoonal processes drive chlorophyll production to be at

its peak along the northernmost AS and along the coast of the Arabian Peninsula (Wiggert et al. 2005).

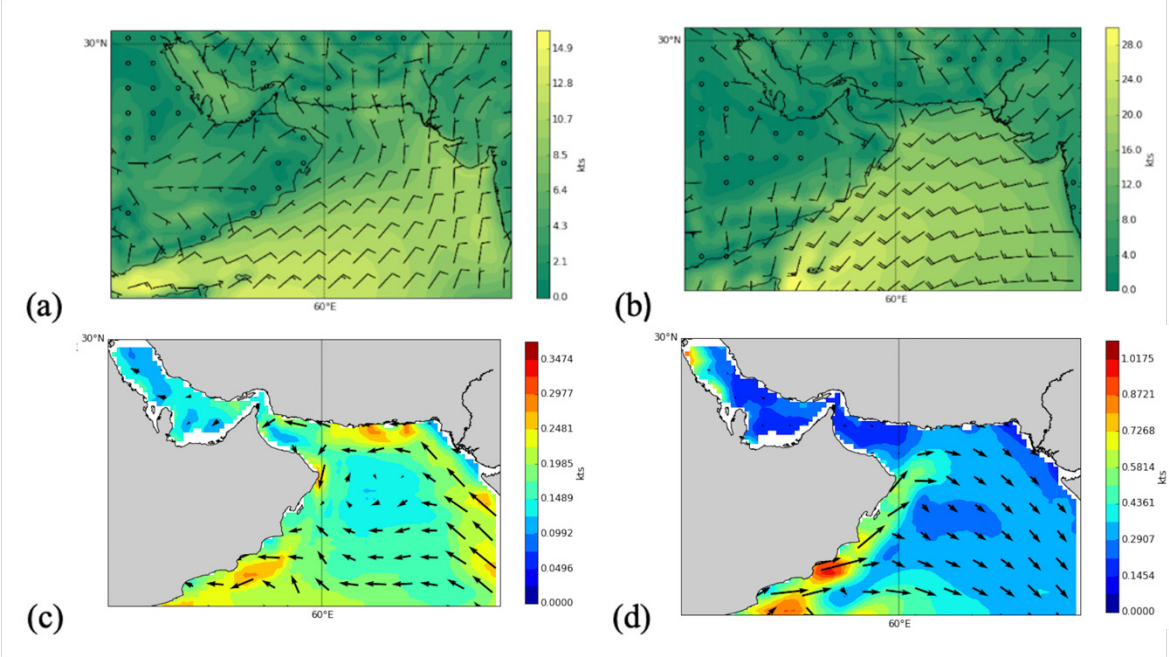

(a) & (b) Climate Forecasting System Reanalysis (CFSR) Evaporation Duct Climatology showing the mean wind speed and direction at 10m above the surface for 1993 to 2010. (c) & (d) CFSR Ocean Data showing the mean current speed and direction at 5m depth for 1993 to 2010. (a) & (c) Northeast monsoon: December-February. (b) & (d) Southwest monsoon: June-September. Of note, color scales between images are different to best represent the monsoon seasons.

Figure 2. CFSR mean wind speed (NOAA/NCEP 2010a) and current (NOAA/NCEP 2010b). Source: NOAA/NCEP

Coastal upwelling caused by offshore Ekman transport brings nutrient rich water to the surface. In one study by Jayaram et al. (2010), satellite observed SST data was used from 1988–2007 to determine the dynamics of coastal upwelling in the southeastern AS. The data showed an increase in SST from 1992–1998 and 2004–2007 with increased upwelling occurring in 1989, 1996, and 2002–2003 (Jayaram et al. 2010). An increase of 0.4°C in SST was noticed in the eastern AS north of 12°N (Jayaram et al. 2010). While upwelling is commonly a phenomenon associated with the southwest monsoon, it has been noticed that at 8°N the offshore Ekman transport (ET) is as strong in the winter as it is in the summer months (Jayaram et al. 2010). The fluctuations in SST are correlated to global

climatic events which include the El Nino Southern Oscillation (ENSO) and Indian Ocean Dipole (IOD). During the 2016–2017 ENSO, a strong negative IOD phase was observed in 2016 and a weak positive one in 2017 (Jayaram et al. 2010). This event is mentioned because of the effect it has on the wind-sea interaction and subsequently the change in the AS' SST. The strong El Nino and extreme negative IOD events of 2016 had a very different effect than the events of 2017. In 2016, the AS experienced a slight increase in the seasonal cycle of SST when compared to 2017 (Khan et al. 2021). Even with this overall increase, there was a decrease of 1°C during the AS summer months due to the strong upwelling along Oman's coast caused by the stronger winds (Khan et al. 2021). This study depicts the influence of ENSO and IOD on the AS' water temperature and upwelling which in turn affects the primary production cycle in the area. A basic understanding of these global processes may explain why recent *c. orsini* blooms in the region are occurring more.

1. 2002 Bloom

Daryanabard and Dawson (2008) studied and attempted to explain the cause of the massive bloom in the Persian Gulf, AS, and GOO which lasted from May to December 2002. Their study stated that *c. orsini* are indigenous to this area and are typically found in the region. The bloom studied by Daryanabard and Dawson (2008) peaked in August 2002 and was the first recorded large-scale bloom for *c. orsini* species. However, its quick onset, offset, and variation in spatial abundance were comparable to other types of jellyfish blooms in the region (Daryanabard and Dawson 2008). Daryanabard and Dawson (2008) collected trawl data on the jellyfish density in August 2002 and 2003 from 25°26'N, 58°55'E to 24°48'N, 61°30'N and recorded the *c. orsini* distribution in the GOO as reported by local fishermen (see Figure 3). The origination of the bloom may have occurred along the Iranian coast with the monsoonal flow transporting the *c. orsini* into the GOO or along the Omani coast; however, there is no trawl data for this area to verify it. During their 2003 cruise, it was noted that the jellyfish density was significantly reduced (Daryanabard and Dawson 2008). The present study has found that the bloom occurred in a year of relatively normal SST and that the bloom was not a result of local coastal degradation or eutrophication, as it was so widespread (Daryanabard and Dawson 2008).

However, the three out of the four preceding years contained the warmest SST recorded since 1982 (Daryanabard and Dawson 2008). The warm SSTs due to the region's natural climate cycle were hypothesized but not confirmed to be the cause of the bloom. (Daryanabard and Dawson 2008).

2. 2020 Bloom

The 2020 bloom originated off Pakistan's coast in February 2020 and the jellyfish were found in high density along Oman's coast and offshore waters until June 2020. Figure 3 depicts the general location of the bloom and its origination. The highest concentrations were found in the northern part of the box (T. Davis 2022, personal communication).

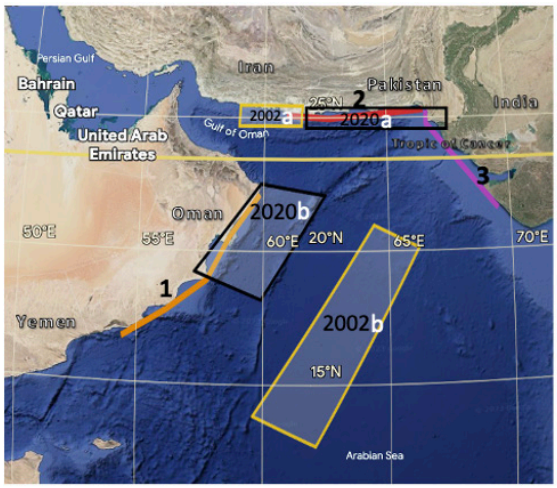

1 (orange line):
16°57'N, 54°40'E
22°25'N, 59°52'N

2 (purple line):
21°32'N, 69°10'E
25°18'N, 66°40'N

3 (red line):
25°50'N, 66°19'E
24°50'N, 61°00'N

The transparent polygons show approximate locations of the two major c. orsini blooms. The coastline segments for the ET calculations are shown as orange, purple and red lines for segments 1, 2 and 3, respectively with their geographical extents shown in the inset. The "a" letter denotes where the blooms originated and the "b" letter is where the blooms were observed.

Figure 3. The study region and *c. orsini* bloom locations. Source: Google Earth

Comparison of the oceanographic conditions in 2002 to 2020 is pivotal in determining the cause of the *c. orsini* bloom. Changes in the oceanographic conditions and its influence on the region's marine ecosystem can hold the key to predicting future blooms. Prediction of these blooms would allow for naval warfighters to be better prepared when conducting operations. To analyze the changes in the region's oceanographic condition,

environmental data from 1993 to 2021 was downloaded from Copernicus Marine Environment Monitoring Service (CMEMS). It is hypothesized that the monsoon-driven enhanced upwelling and heightened convective mixed layer resulted in increased nutrient availability fueling the food chain from mixed diatoms to *n. scintillans* to *c. orsini.*

THIS PAGE INTENTIONALLY LEFT BLANK

II. DATA

Data used in this experiment was retrieved from the Copernicus Marine Environment Monitoring Service (CMEMS) with each of the following products described below. CMEMS provides free global and regional data funded by the European Commission and employed by Mercator Ocean International. The products utilized from CMEMS include Global Ocean Physics Reanalysis, Global Ocean Physics Analysis and Forecast, Global Ocean Biogeochemistry Hindcast, Global Ocean Biogeochemistry Forecast and Analysis, and Global Ocean Blended Wind Reprocessed and Observed. All data is of scientific quality which is labeled as processing level 4 (L4).

Of note, the U.S. Navy's Hybrid Coordinate Ocean Model (HYCOM) data was unavailable for the dates and region needed.

A. GLOBAL OCEAN PHYSICS REANALYSIS

Sea water potential temperature, northward and eastward sea water velocity, sea surface height above the geoid, and ocean mixed layer thickness defined by sigma theta from the surface to the bottom for January 1 1993 to December 31 2020 were obtained from a global eddy-resolving reanalysis model, GLORYS12V1. The model has a horizontal resolution of 1/12° and 50 vertical depth (z) levels using an Arakawa C native grid (CMEMS 2018d). The 50 z levels range from 0 to 5500m. The model component, NEMO 3.1, begins at the surface with model initialization by the European Centre for Medium Range Weather forecast reanalysis (ECMWF-ERA). A reduced-order Kalman filter processes the observations which include Reynolds 0.25° Advanced Very High-Resolution Radiometer (AVHRR) for SST, satellite altimetry for sea level anomaly (SLA), and in-situ temperature/salinity (T/S) profiles from CMEMS Coriolis Ocean Dataset for Reanalysis (CORAv4.1) database (CMEMS 2018d). T/S measurements are obtained from many different sources, from research vessels to autonomous platforms. A three-dimensional variational assimilation (3D-VAR) scheme offers improvement for the large-scale biases in both measurements (CMEMS 2018d). World Geodetic System (WGS 84) is the coordinate reference system with this product using the daily mean for temporal

resolution. Bathymetry input for deep ocean is ETOPO1 and GEBCO8 on the coast and continental shelf. ETOPO1 is the 1-arc-minute Global Relief Model developed by NOAA. GEBCO8 is the General Bathymetric Chart of the Ocean and contains a 30-arc second spatial resolution. The product user manual (Drevillon et al. 2018) contains more details about the dataset.

B. GLOBAL OCEAN PHYSICS ANALYSIS AND FORECAST

Sea water potential temperature and ocean mixed layer thickness defined by sigma theta from the surface to the bottom for January 1 2021 to December 31 2021 were obtained from a global Mercator global ocean analysis and forecast model, GLO12v4, has a horizontal resolution of 1/12° and 50 vertical z levels using an Arakawa C native grid (CMEMS 2016). The 50 depth levels range from 0 to 5500m. The ocean model component of GLO12v4, the forecast system name, utilizes NEMO 3.6, which is the model component of the system. Bathymetry input for deep ocean is ETOPO1 and GEBCO8 on the coast and continental shelf. A reduced-order Kalman filter processes the observations derived from a Singular Evolutive Extended Kalman (SEEK) filter using a 3D-VAR bias correction and incremental analysis update (CMEMS 2016). SST are L3S from ODYSSEA which is an interpolated "multisensor gridded 0.02° resolution super-collated product" (NOAA Coastwatch 2022), SLA from AVISO which is satellite altimetry data, and T/S profiles from the CORA database (CMEMS 2016). The daily data files used include sea water potential temperature and ocean mixed layer thickness defined by sigma theta from the surface to the bottom for January 1 2021 to December 31 2021. The product User's Manual (Le Galloudec et al. 2016) gives more information about the dataset.

C. GLOBAL OCEAN BIOGEOCHEMISTRY HINDCAST

Daily mean chlorophyll-a data from the surface to the bottom for January 1 1993 to December 31 2020 was obtained from a Mercator-ocean global ocean biochemical multi-year product. It uses a standard collocated grid with 1/4° resolution and 75 standard levels (CMEMS 2018c). It is interpolated from the 1/12° and 50 vertical levels Arakawa C native grid. The 75 levels range from 1m near the surface to 200m depth. This product uses the PISCESv2, biochemical model, available on the NEMO 3.6, modeling platform.

NEMO 3.6 uses daily fields from the ocean forcings numerical simulation, FREEGLORYS2V4, produced at Mercator-Ocean and atmospheric forcings from ERA-Interim reanalysis produced at ECMWF. There is no data assimilation for this product (CMEMS 2018c). Bathymetry input for deep ocean is ETOPO1 and GEBCO8 on the coast and continental shelf. European Terrestrial Reference System 1989 (ETRS89) is the coordinate reference system. The product User's Manual (Le Galloudec et al. 2018) gives more information about the dataset.

D. GLOBAL OCEAN BIOGEOCHEMISTRY ANALYSIS AND FORECAST

Daily mean chlorophyll-a data from the surface to the bottom for January 1 2021 to December 31 2021 was obtained from a global Mercator global ocean biogeochemical sliding two-year product, produced by CMEMS. It uses a 1/4° horizontal resolution, equirectangular grid, and 50 vertical levels ranging from 0 to 5500m in depth (CMEMS 2018b). This product uses the PISCES, biochemical model, available on the NEMO 3.6, modeling platform. The data assimilation scheme is SEEK with observations processed from the OCEANCOLOUR_GLO_BGC_L4_NRT_009_102 dataset. This is a near real time (NRT) dataset (CMEMS 2018b). Bathymetry input for deep ocean is ETOPO1 and GEBCO 2014 on the coast and continental shelf. Lamouroux and Tonani (2018) provide additional information about this dataset.

E. GLOBAL OCEAN WIND PRODUCTS

Reprocessed wind fields at 10m are used for January 1 1993 to December 31 2019 was derived from satellite scatterometers to include ASCAT-(Advanced Scatterometer), ASCAT-B, SCATSAT (Scatterometer Satellite), and HY-2B (Hai Yang 2B, 2019 only) and ancillary remote sensing to include SSMIS (Special Sensor Microwave Imager Sounder) and WINDSAT (CMEMS 2019). The data is aligned with the synoptic forecast times at every 6 hours. Reprocessing occurs using near real time scatterometers and radiometer data along with the ECMWF-ERA and ECMWF-ERA5, 5th generation of ERA, for 2019 (CMEMS 2019). Wind products use a regular grid with 1/4° spatial resolution. NRT observation wind fields are used for January 1 2020 – December 31 202, using 6-hourly wind products derived from ASCAT-A and ASCAT-B along with ancillary

remote sensing using SSMIS (CMEMS 2018a). Processing level and spatial resolution remains unchanged between the reprocessed and NRT observations. More information can be found in the product user manuals for reprocessed data (Giesen et al. 2019) and NRT data (Giesen 2018).

III. METHODS

A. EKMAN TRANSPORT

Ekman transport was calculated for three distinct coastlines in the region to determine the upwelling indices. The coastlines were chosen based on two factors: (1) consistent and distinct orientation of the coastline segments in relation to the monsoonal winds and (2) known or hypothetical location of the jellyfish blooms in 2002 and 2020. Figure 3 depicts each of the three regions. The following equations were used for the ET calculations:

$$U_{EK} = \frac{\tau^y}{\rho f} \tag{1}$$

$$V_{EK} = \frac{\tau^x}{\rho f} \tag{2}$$

where τ^y is the northward wind stress component, τ^x is the eastward wind stress component, $\rho = 1025\,\mathrm{kg/m^3}$ is the seawater density, $f = 2\Omega\sin(\varphi)$ is the Coriolis parameter, U_{EK} is the eastward ET, and V_{EK} is the northward ET. The angle for each of these coastlines was calculated using a 50km resolution for each year from 1993 to 2021. The corresponding along-shore and cross-shore ET components were then calculated for each 50-km long chunk and integrated for each of the three coastline segments shown in Figure 3. Additionally, in the northern hemisphere, ET occurs 90° to the right of the wind direction. Upwelling occurs when ET is positive (offshore) with water moving away or diverging from the coast causing cooler and nutrient-rich deep water to rise, replacing the transported surface water. Downwelling occurs when ET is negative with water moving or converging toward the coast causing warm surface water to sink.

B. EMPIRICAL ORTHOGONAL FUNCTIONS

To detect dominant patterns of oceanic variability and potential drivers and/or triggers of the jellyfish blooms, an Empirical Orthogonal Function analysis (EOF) was applied to the daily time-series of the two-dimensional map of the oceanographic characteristics. The EOF approach (Thomson and Emery 2014) reduces dimensionality of

large time and space dependent fields of oceanographic characteristics and separates their temporal and spatial variability. The fields are represented as a linear decomposition of orthogonal spatial maps (eigenmodes, hereafter EOFs) with time-dependent coefficients (principal components, hereafter PCs). The EOFs are independent from each other and arranged according to their contribution into the field variability. Lowest modes have the largest spatial scales and are the main contributors to variability. The EOF analysis is a statistical method and does not guarantee that each EOF will have an unambiguous dynamic interpretation. However, it shows the inter-relationship between the most important and larger scale spatial patterns of different oceanographic characteristics and to other climatological modes of variability. The following equation is a mathematical formulation of EOF decomposition where ψ is a variable, *x, y* are latitude and longitude, and *t* is time:

$$\psi(x, y, t) = \sum_{i=1}^{N=5} EOF_i(x, y) * PC_{\mathrm{i}}\,(t) \tag{3}$$

The Z. Chunlue (2023) Empirical Orthogonal Function (EOF) analysis software was used for the EOF analysis.

EOF analysis was utilized on the region in Figure 3 from 1993 to 2020. The analysis method was applied to surface temperature, mixed layer depth, and surface chlorophyll-a and their respective actual values, means, and anomalies. Anomalies were calculated as deviations of actual values from their respective means over the analyzed time period. Five EOFs were used for each of the variables which represent the most significant modes of variability. An example of the EOF decomposition for the mixed layer depth is shown in Figure 14. For each EOF, the left panel shows the spatial map called the EOF and the right panel represents the PC time series. Multiplying the spatially dependent EOF values by its corresponding PC time series allows for spatial patterns of variability to be recognized and compared over a certain time frame. The data used has been detrended. Each of the PCs and EOFs have been normalized by their corresponding variances in Table 1 with the sign reversed for chlorophyll-a and temperature. Using EOF provides comparison by year and season to recognize if a particular signal was stronger, weaker, or neutral thus influencing temperature, mixed layer depth, or chlorophyll-a concentrations in a particular area.

C. ANALYSIS OF POTENTIAL PREDICTORS

Temperature was analyzed for all depths for the EOF calculations and only at the surface (0.5m) for other temperature analyses. Temperature and mixed layer depth were compared to their corresponding anomalies. Anomalies provide the best insight of how a particular day compares to the total 29-year average for that day. Mixed layer depth is not a function of depth and was used the same for all calculations. Temperature and mixed layer depth used daily mean values from January 1, 1993, to December 31, 2021. For chlorophyll-a, only daily mean surface data (0.5m) was examined for January 1, 1993, to December 31, 2021, for both the EOF analyses. Since chlorophyll-a concentrations exhibit significant patchiness and discrete and large spatial gradients, we used the $\log_{10}$ of the actual concentrations to visualize and analyze it. Surface temperatures were used as *c. orsini* are most abundant on the surface and are negligible at depths below 75m (Daryanabard and Dawson 2008).

THIS PAGE INTENTIONALLY LEFT BLANK

IV. RESULTS

When analyzing the two years of *c. orsini* blooms, the timeframes during the year in which they occur in high concentration were different. In 2002, the blooms began in May 2002 and concluded by December 2002 (Daryanabard and Dawson 2008). In 2020, the blooms began in February 2020 and concluded by June 2020. Additionally, their origination locations differed. As described in the introduction, the bloom origination in 2002 is not conclusive whereas, the 2020 bloom is known to have originated along Pakistan's coast. The timeframe and bloom locations are crucial when studying the results.

A. PRELIMINARY RESULTS

As mentioned in the introduction, the regional oceanographic and meteorologic patterns are driven by the monsoon seasons. Compared to all 29 years, the two years of jellyfish bloom interest, 2002 and 2020, depict a regime that is similar to a typical year.

Below the actual temperature and chlorophyll values during the blooms are compared. In Figure 4, chlorophyll values and anomalies are compared at 1200 UTC on August 8, 2001, 2002, 2003, and 2020., This date is chosen as Daryanabard and Dawson (2008) collected trawl data on the jellyfish density in August 2002 and 2003 from 25°26'N, 58°55'E to 24°48'N, 61°30'N. Furthermore, they noticed that the jellyfish density was reduced significantly in 2003 at this location. Chlorophyll anomaly is highest and most spatially abundant in 2002. This higher concentration coupled with the southwest monsoonal wind pattern could provide reasoning behind why the *c. orsini* bloom occurred. Higher chlorophyll concentration maybe a result of increased upwelling that occurred in 2002; as described in the ET results section. Figure 5 shows the chlorophyll values and anomalies for February 6, 2002, 2019, 2020, and 2021. Comparing the four years, there is an increase in chlorophyll concentration in 2020 however, 2021 had a much more anomalous amount of chlorophyll in the region. In 2021 there was not a bloom, therefore, these images do not lend support to chlorophyll being the only contributing factor for a bloom occurring as chlorophyll concentration was abnormally high in 2021.

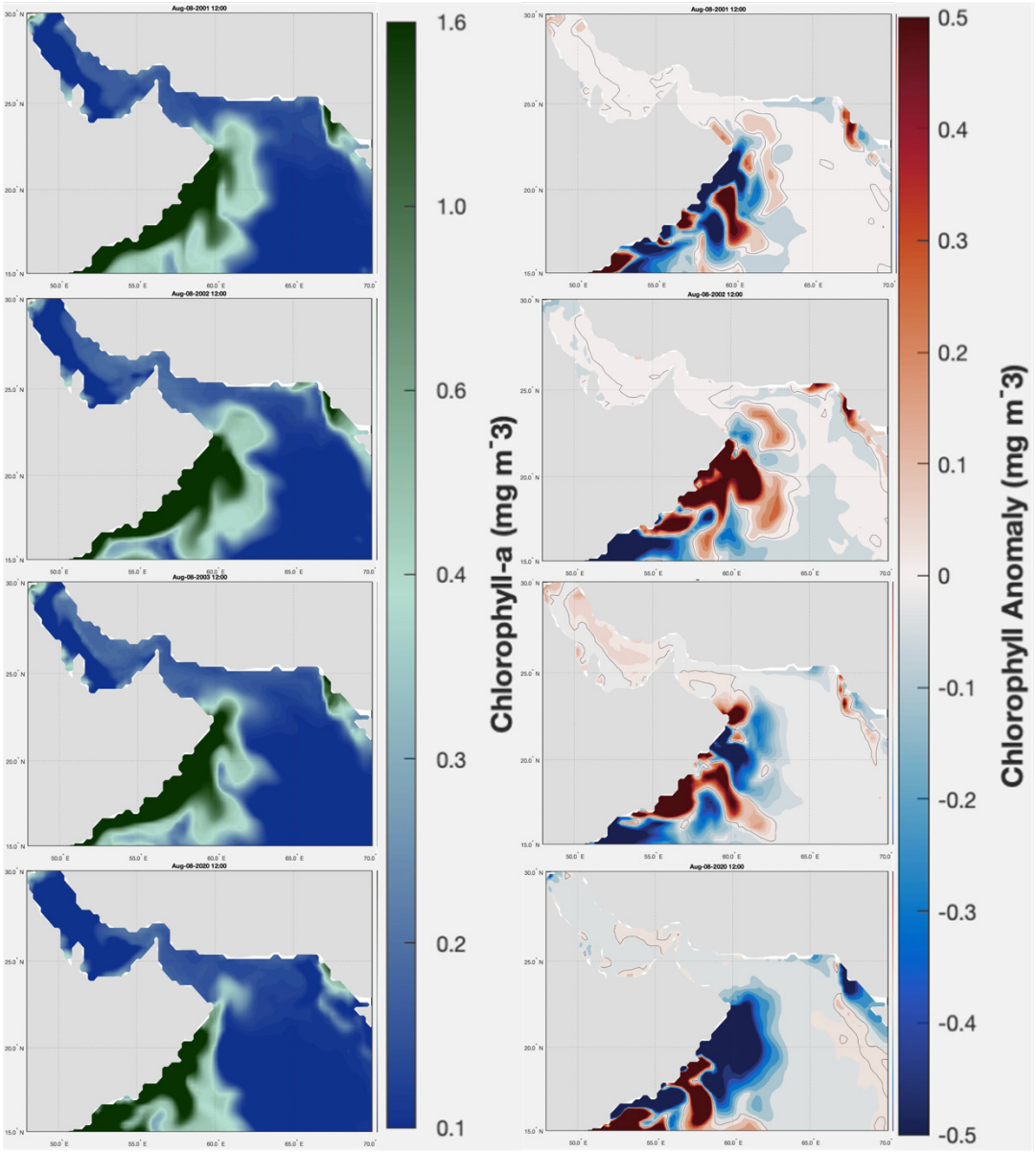

Black line in the anomaly plot represents the zero contour.

Figure 4. Chlorophyll-a concentration and the corresponding anomaly for 1200 UTC on August 8, 2001, 2002, 2003, and 2020 (top to bottom)

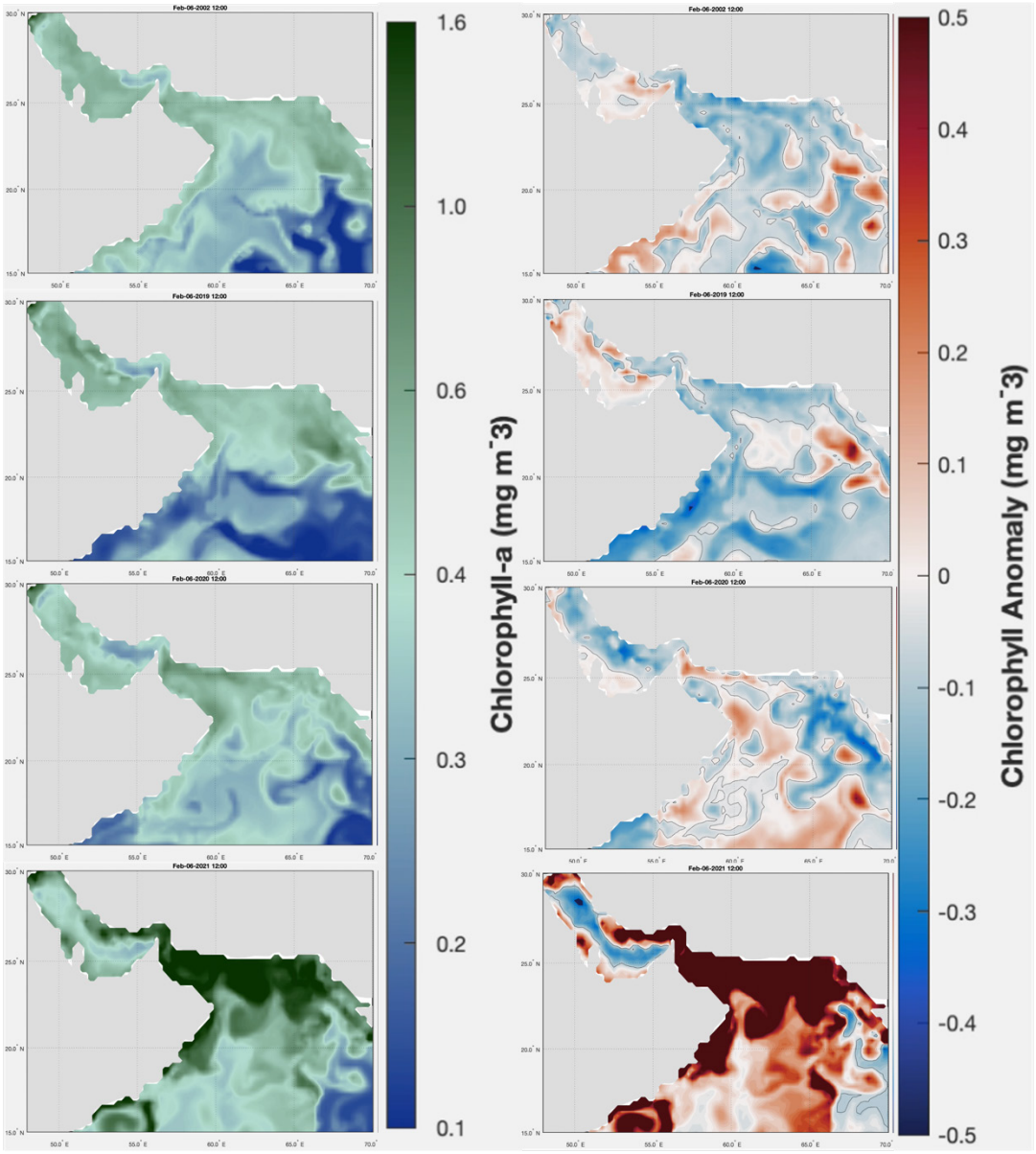

Black line in the anomaly plot represents the zero contour.

Figure 5. Chlorophyll-a concentration and the corresponding anomaly for 1200 UTC on February 6, 2002, 2019, 2020, and 2021(top to bottom)

Figure 6, depicts 1200 UTC on August 8, 2001, 2002, 2003, and 2020 temperature values and anomalies are compared. The 2002 image lends support that upwelling occurred along Oman's coast with follow on images showing the cool, deeper water being transported northward. Comparatively, the GOO remained cooler than average until October when the water warmed from both the north and south. After the monsoon

transition season, December's water was cool again. The temperature dynamics in 2002 depict a fluctuation in SST by the monsoonal wind. The change in wind and extreme warming/cooling of the water provides support for the jellyfish blooms decreasing in December 2002.

Furthermore, Figure 7 shows the temperature values and anomalies for 1200 UTC on February 6, 2002, 2019, 2020, and 2021. In 2020, upwelling is evident along Pakistan's coast but is more spatially vast and stronger compared to 2019 and 2021. The upwelled waters are transported southwestward via the northeast monsoon wind regime and currents (see Figure 2 & 23). As transition season occurs, the beginning of April brings warmer water into the region from the south. By June 2020, the region is approximately 3ºC warmer. Again, this increase in temperature lends support to the jellyfish bloom concentration decreasing as the conditions needed for rapid jellyfish reproduction diminish.

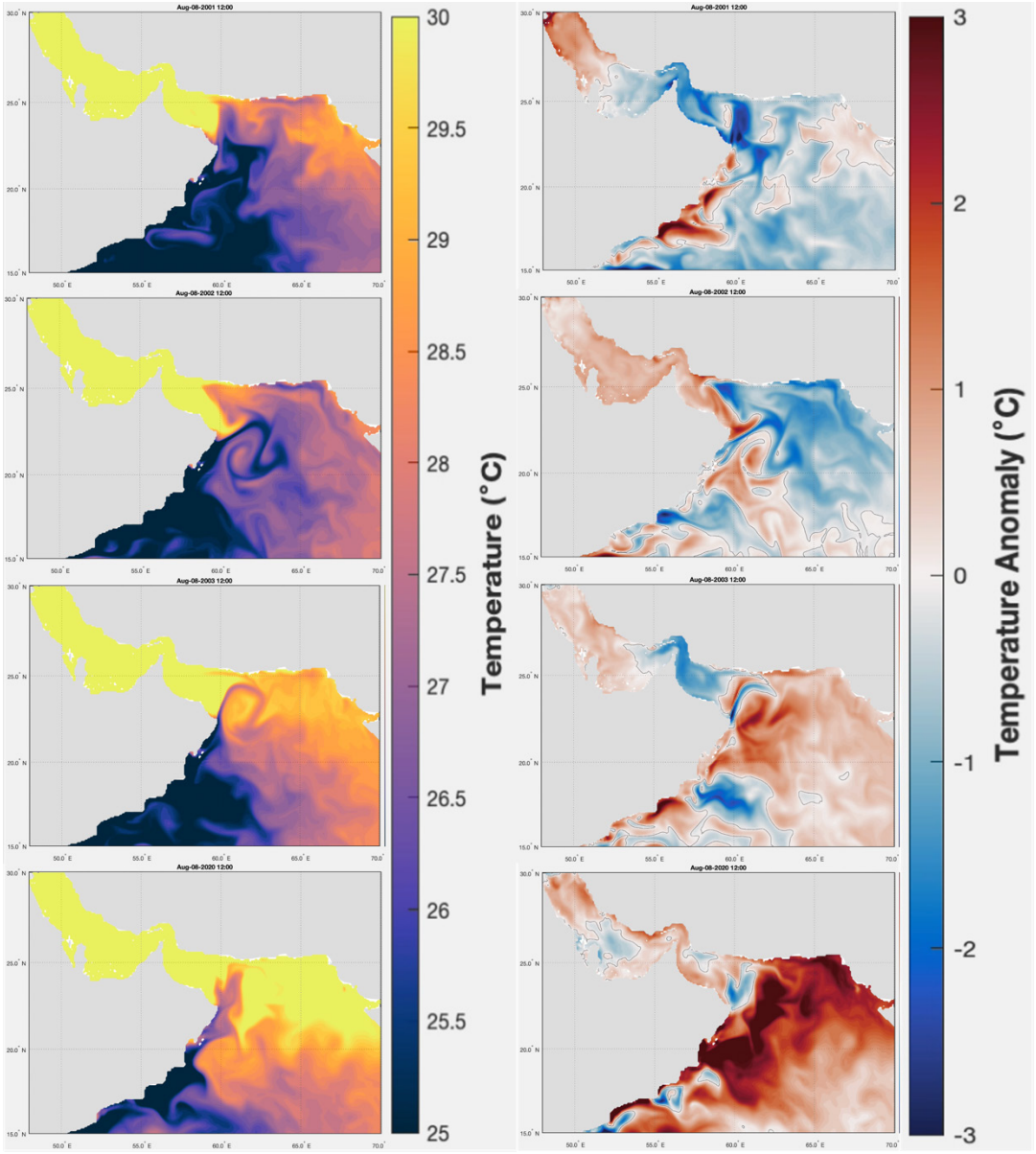

Black line in the anomaly plot represents the zero contour.

Figure 6. Temperature and the corresponding anomaly for 1200 UTC on August 8, 2001, 2002, 2003, and 2020 (top to bottom)

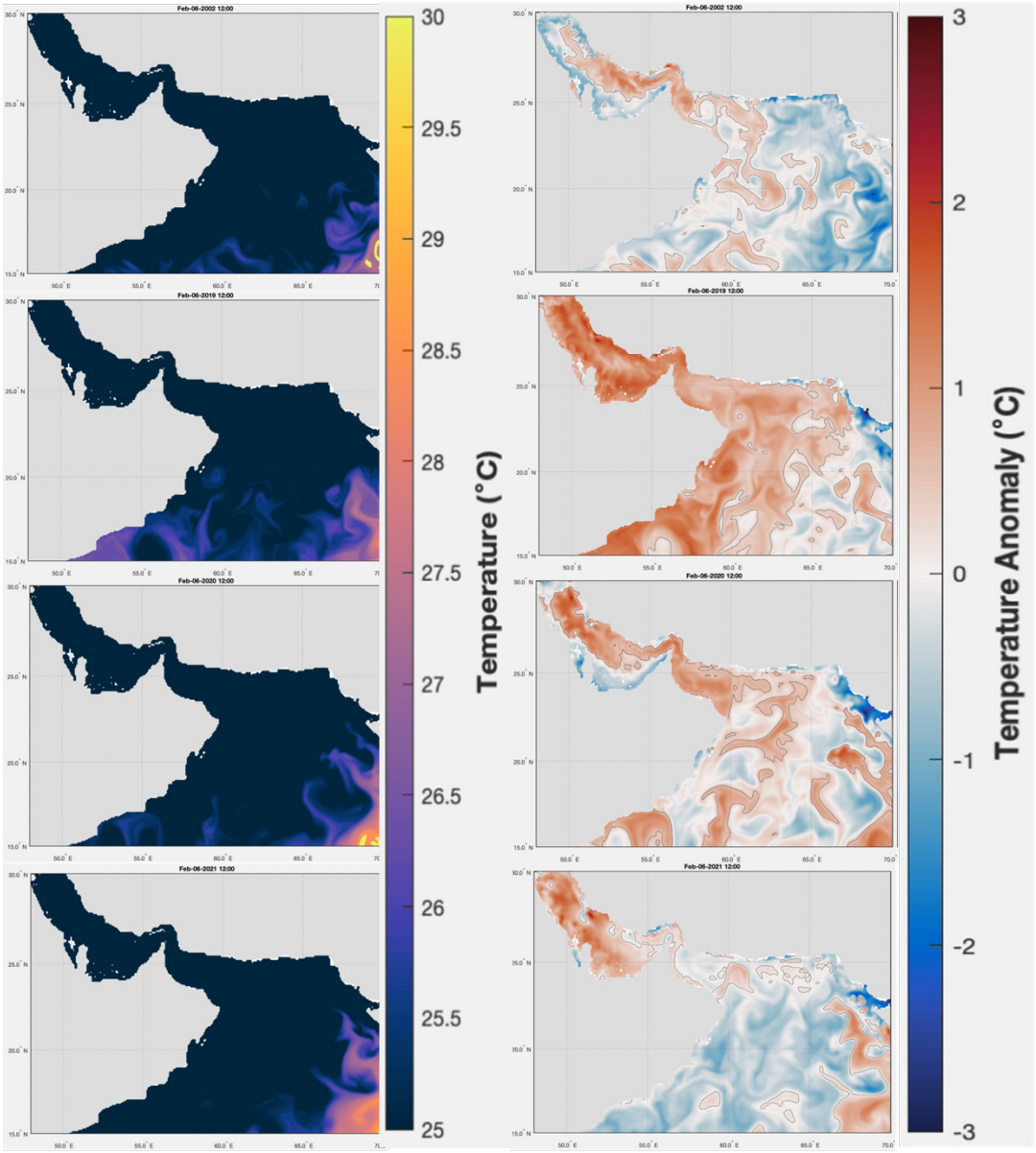

Black line in the anomaly plot represents the zero contour.

Figure 7. Temperature and the corresponding anomaly for 1200 UTC February 6, 2002, 2019, 2020, and 2021(top to bottom)

B. EKMAN TRANSPORT

In Figure 8, 1200 UTC on August 8, 2001, 2002, 2003, and 2020 are compared. Again, this date was chosen as described in the preliminary results and to provide uniformity when understanding the oceanographic processes in the region. In each of the four years, upwelling is strong along the coast of Oman which aligns with the monsoonal

southwest wind, that dominants the summer months. Along the coast of Iran, where the *c. orsini* were plentiful in 2002, weak downwelling is present which aligns with the previous and follow-on years. However, this does not support that upwelling in 2002 along the Irani coast was a contributing factor to the bloom. The upwelling along the Omani coast was strongest in 2002 compared to the other 3 years. The monsoonal southwest wind could bring the upwelled nutrient-rich water along the Omani coast across the GOO leading to increased primary production and thus to a surplus of food available for the *c. orsini* jellyfish to feed on.

Figure 9 shows the ET for 2020 as 1200 UTC on February 6, 2002, 2019, 2020, and 2021 are compared. The bloom in 2020 originated off the Pakistani coast in February 2020, with *c. orsini* found in overwhelming numbers to the southwest in the GOO (see Figure 3). The positioning of the bloom aligns with the monsoonal northeast wind regime which dominates the winter months. In both 2019 and 2020, there is significant upwelling along Pakistan's coastline. The 2019 conditions will be further explained in the correlations results. Again, the nutrient rich water being upwelled combined with the northeasterly wind and current flow would provide sustenance for the *c. orsini* to bloom throughout the gulf. This upwelling pattern along the eastern side of the GOO prevails until late June with the shift of the monsoon season. This upwelling/downwelling pattern is like other years, however, the magnitude of 2020s upwelling is notable.

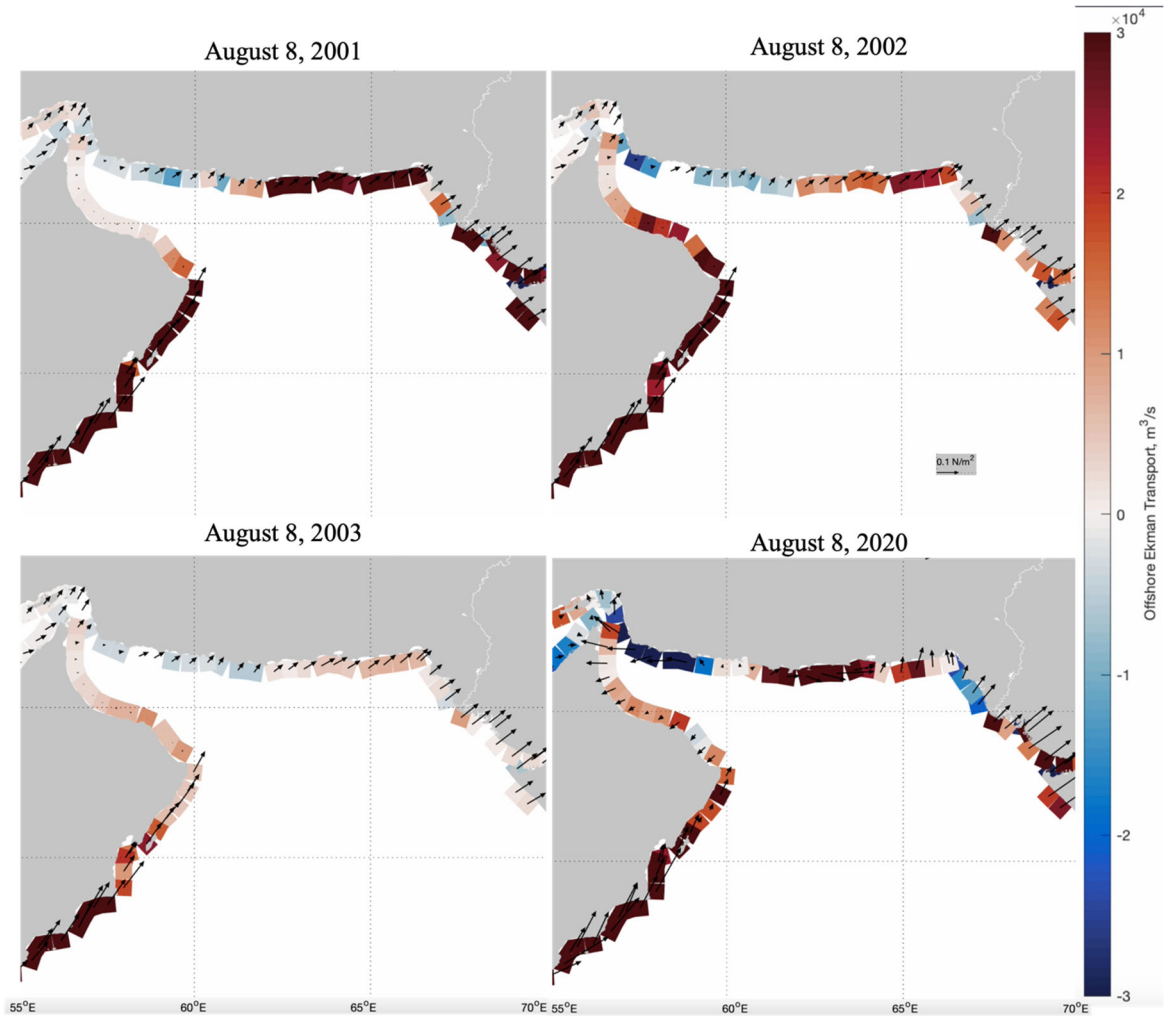

The positive values (red color) correspond to upwelling-favorable conditions. The negative values (blue color) correspond to downwelling-favorable conditions. The arrows represent the total wind-stress [N/m^2] at the 10 m height. For: (a) 1200 UTC on February 6, 2002, 2019, 2020, and 2021

Figure 8. The integrated offshore Ekman transport [m^3/s] for 50-km coastline segments at 1200 UTC on August 8, 2001, 2002, 2003 and 2020

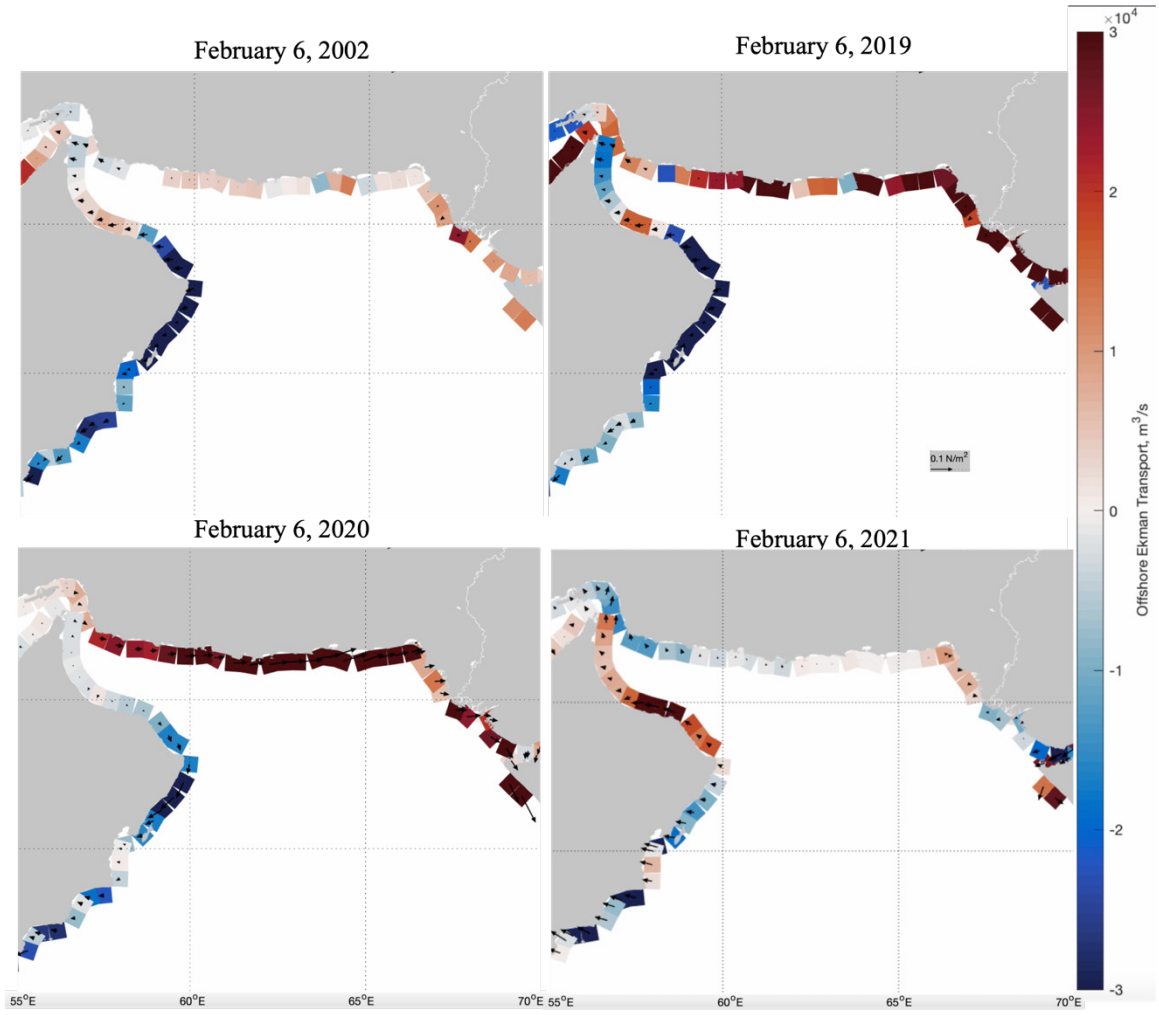

The positive values/red color correspond to upwelling-favorable conditions. The negative values/ blue color correspond to downwelling-favorable conditions. The arrows represent the total wind-stress [N/m^2] at the 10 m height. For: (a) 1200 UTC on February 6, 2002, 2019, 2020, and 2021

Figure 9. The integrated offshore Ekman transport [m^3/s] for 50-km coastline segments at 1200 UTC on February 6, 2002, 2019, 2020, and 2021

C. EOF

Table 1 is the percent of variance, as explained by each of the first five modes for chlorophyll-a (CHL-A), mixed layer depth (MLD), and surface temperature (TEMP). All the modes summed together provides a total picture of the variability, yet each mode is not dependent on each other. The table depicts how each mode's variance contribution changes when analyzing its value, anomaly, or mean. Note that the first two modes explained at

least 90% of variance for the actual values. Mode 1 accounts for majority of the variability in the region and is further explained in the Correlations section.

Table 1. Distribution of variance explained by the first five EOFs

MODE	CHL-A	MLD	TEMP
1	85.3	77.1	78.7
Anomaly	45.7	61.9	65.7
Mean	91.3	81.8	80.1
2	6.3	16.6	18.8
Anomaly	25.1	17.6	15.8
Mean	4	16.4	18.7
3	4	2.7	1.3
Anomaly	14.1	9.3	8
Mean	3.3	1	0.73
4	2.5	2.4	0.77
Anomaly	8.1	7.4	6.6
Mean	1.2	0.58	0.28
5	2	1.2	0.52
Anomaly	7	3.9	3.8
Mean	0.26	0.19	0.14

The first column lists the mode number and its associated anomaly or mean. Columns 2 through 4 list the percentage for CHL-A, MLD, and TEMP and its respective mode's variance.

Figure 10 depict chlorophyll-a's EOFs and their associated PCs. Figure 11 shows EOFs and their associated PCs for long term mean chlorophyll. All five EOFs reflect increase/decrease of surface chlorophyll concentration in the coastal regions of the AS,

predominantly at the Omani coast and, to a much lesser degree, along the northeastern coastal region AS. Time variations, as reflected in the PCs, demonstrate strong monsoonal variability.

EOF1 corresponds to seasonal variations in chlorophyll-a concentrations along the whole Omani coast between $15 - 22^{\circ}N$ (see Figure 10). The pronounced positive phase is observed in June-October. Thus, is confined to the southwest/summer monsoonal season and driven by the nutrient availability due to the enhanced coastal upwelling. The maximum deviation of surface chlorophyll concentration from a long-term mean is observed in August, the peak of the summer monsoon.

The spatial pattern of EOF2 (see Figure 11) exhibits a dipole structure of the chlorophyll concentration along the northern and southern parts of the Omani coast. The positive northern phase (and negative southern phase) are observed in July-October with a peak in September. The negative northern phase (and positive southern phase) are observed in June-September with a peak in July. The positive southern phase leads by about 2 months, which may indicate some contribution from the alongshore advection caused by the SW monsoonal winds.

To better analyze the years 2002 and 2020, Figures 12 and 13 show how the PC and its associated anomaly in comparison to the entire dataset. In both plots, chlorophyll fluctuates during the summer monsoon for all PCs and PC 3–4 has some variation during the winter monsoon. Both 2002 and 2020 follow similar patterns in the previous and follow on years. However, 2002 has a stronger value in PC3 compared to the mean. Whereas 2020 is more unusual with higher values in both PC1 and PC4.

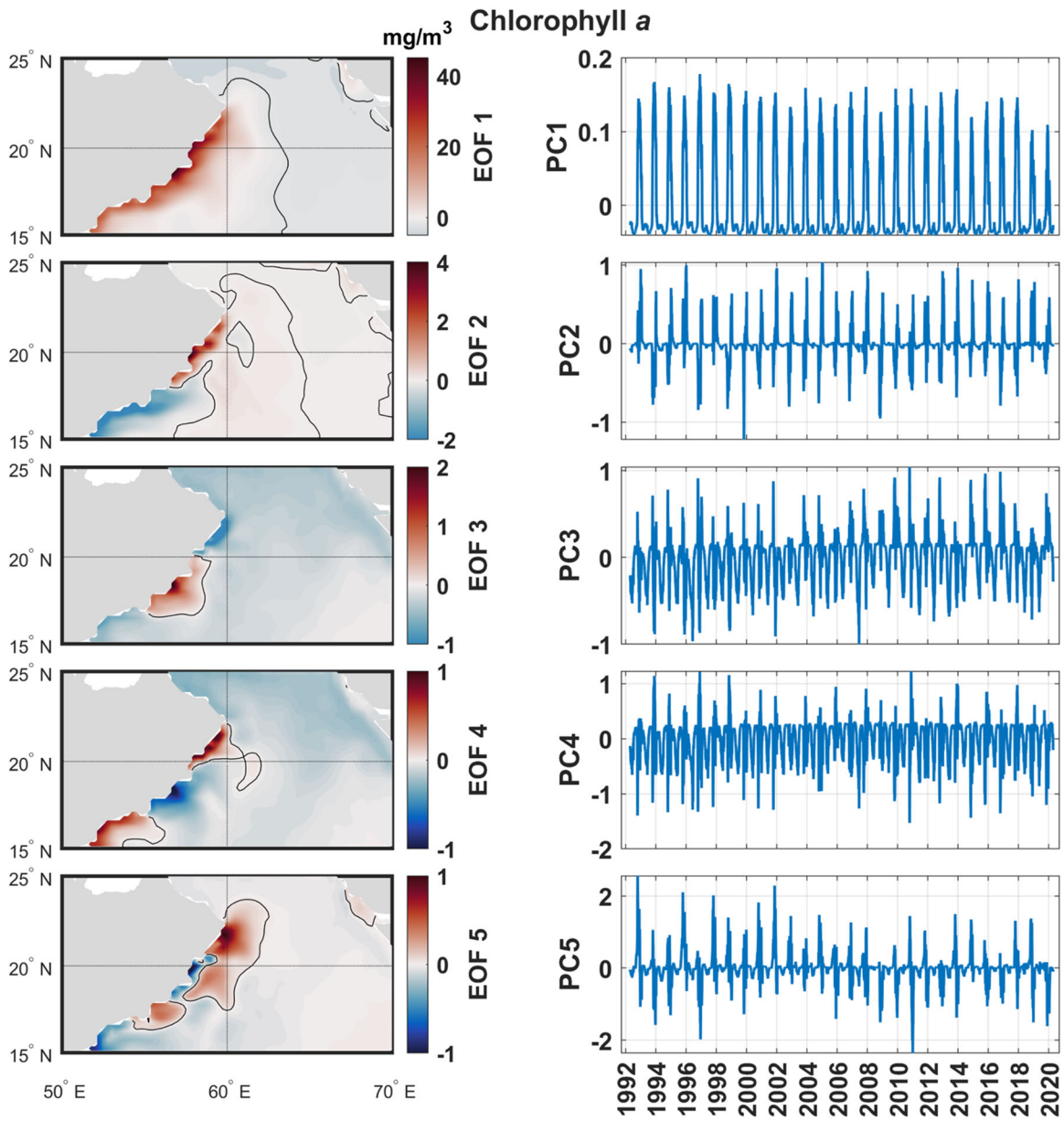

Black line in the EOF plot represents the zero contour.

Figure 10. EOF analysis of the CHL-A concentration at the sea surface for 1993–2020

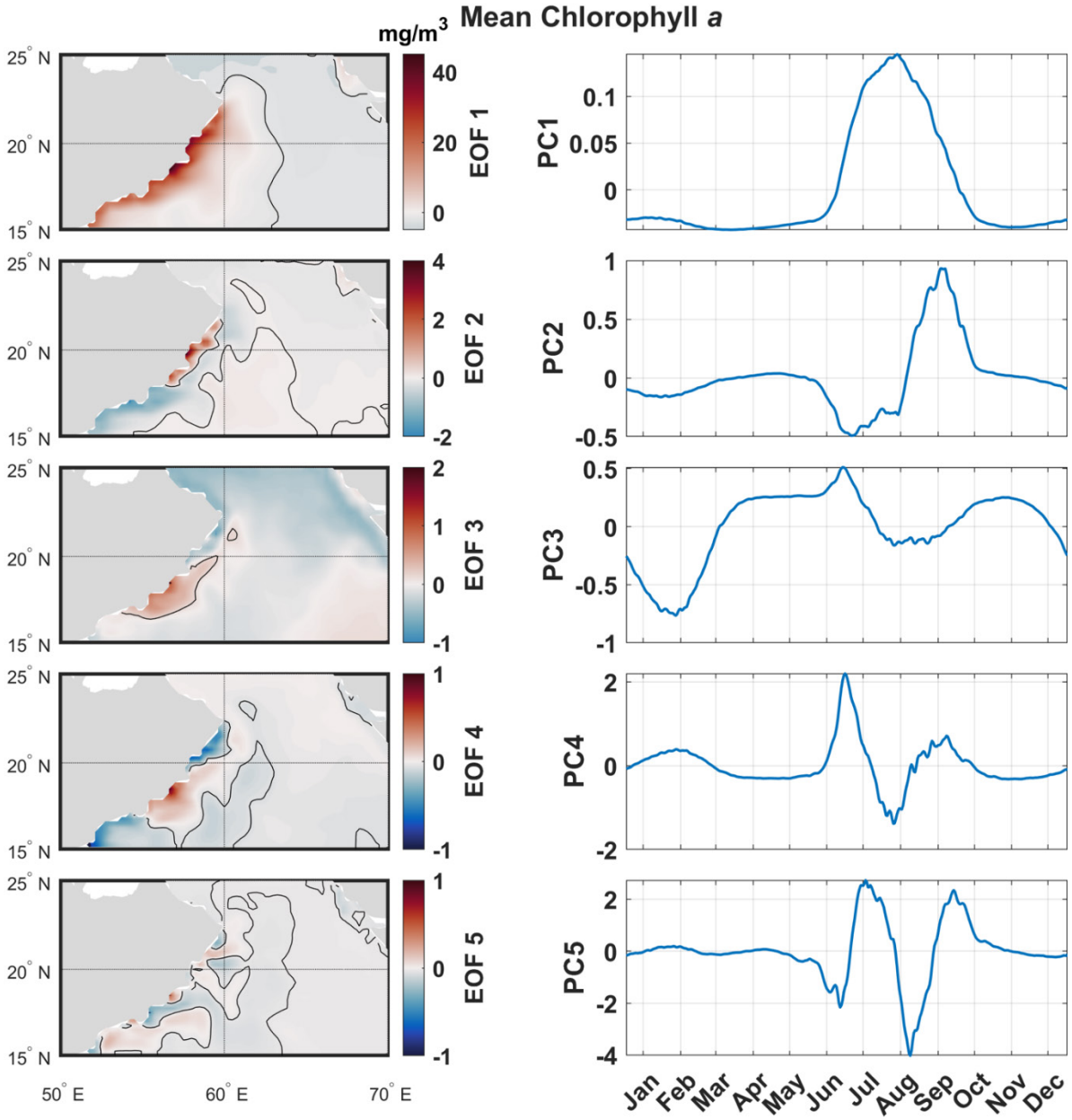

Black line in the EOF plot represents the zero contour.

Figure 11. EOF analysis of the CHL-A mean concentration at the sea surface for 1993–2020

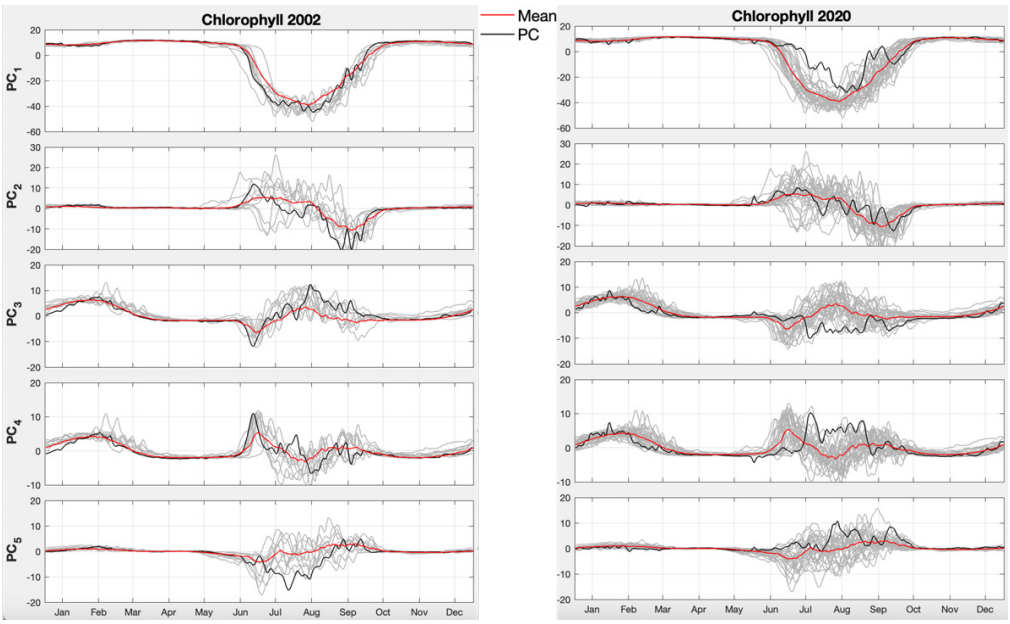

Red line depicts the mean for all years, black line is the PC value for the year listed, and the gray lines are previous years.

Figure 12. Interannual variability of PC for CHL-A in 2002 (left) and 2020 (right)

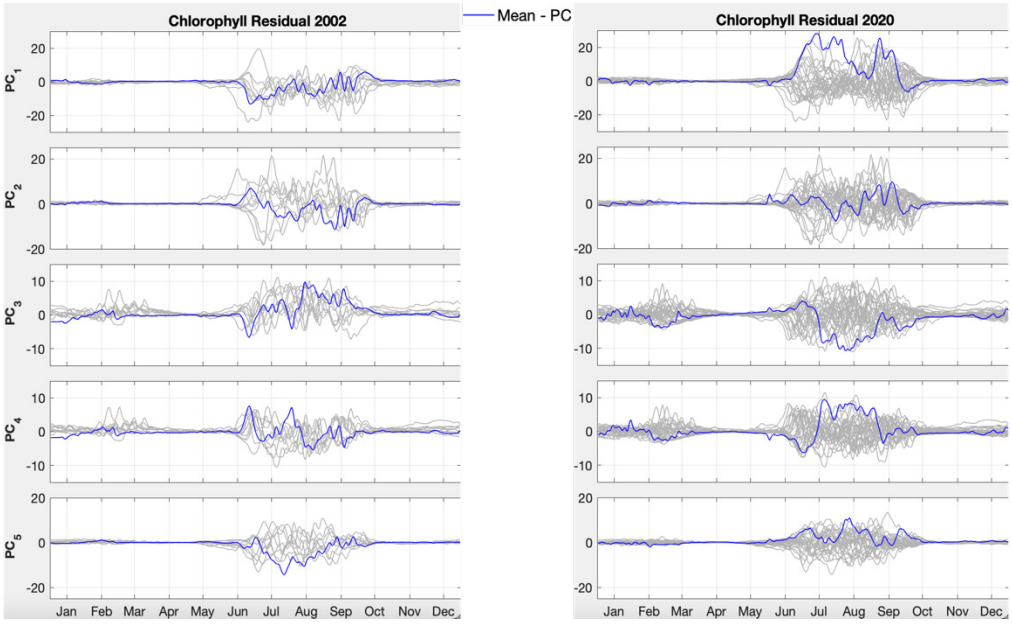

Blue line is difference by subtracting the year's actual PC value from the mean. This allows visualization of the difference of that year from the mean. Gray lines represent previous years.

Figure 13. Interannual variability of PC for CHL-A residual in 2002 (left) and 2020 (right)

Figure 14 depict MLD's EOFs and their associated PCs. Figure 15 shows EOFs and their associated PCs for long term mean MLD. Focusing on the first two modes as they account for over 97% of the total variance. The more positive the EOF is the deeper the mixed layer depth is because of downwelling or enhanced convection. As seen in EOF1 (see Figure 15), the smallest values occur along the Omani coast and the northeastern coastal region AS due to upwelling. This positive anomaly/deepening, maxima, occurs during the northeast monsoon and is connected to wind driven convective overturning of the mixed layer.

The spatial pattern of EOF2 shows a positive value along the coasts and in the GOO with negative values in the open water of the AS (see Figure 14). This pattern is associated with a large-scale ocean circulation that reverses with the change in monsoon season. Hence, why during the minima in July, occurring during the summer/southwest monsoon, these values will now become positive. Additionally, there is a shallow MLD with the onset of the southwest monsoon because of upwelling. These two modes align with the two monsoon seasons in the region. Notably, during the summer monsoon there will be a negative deviation of MLD from its mean along the coasts in mode 2 and negative deviation of MLD from its mean in mode 1 during the transition seasons.

To better analyze the years 2002 and 2020, Figures 16 and 17 show how the PC and its associated anomaly compare to the entire dataset. In both plots, 2002 and 2020 follow similar patterns as in previous and follow-on years. During the blooms' timeframe for each of the respective years, there are no abnormal MLD PC results.

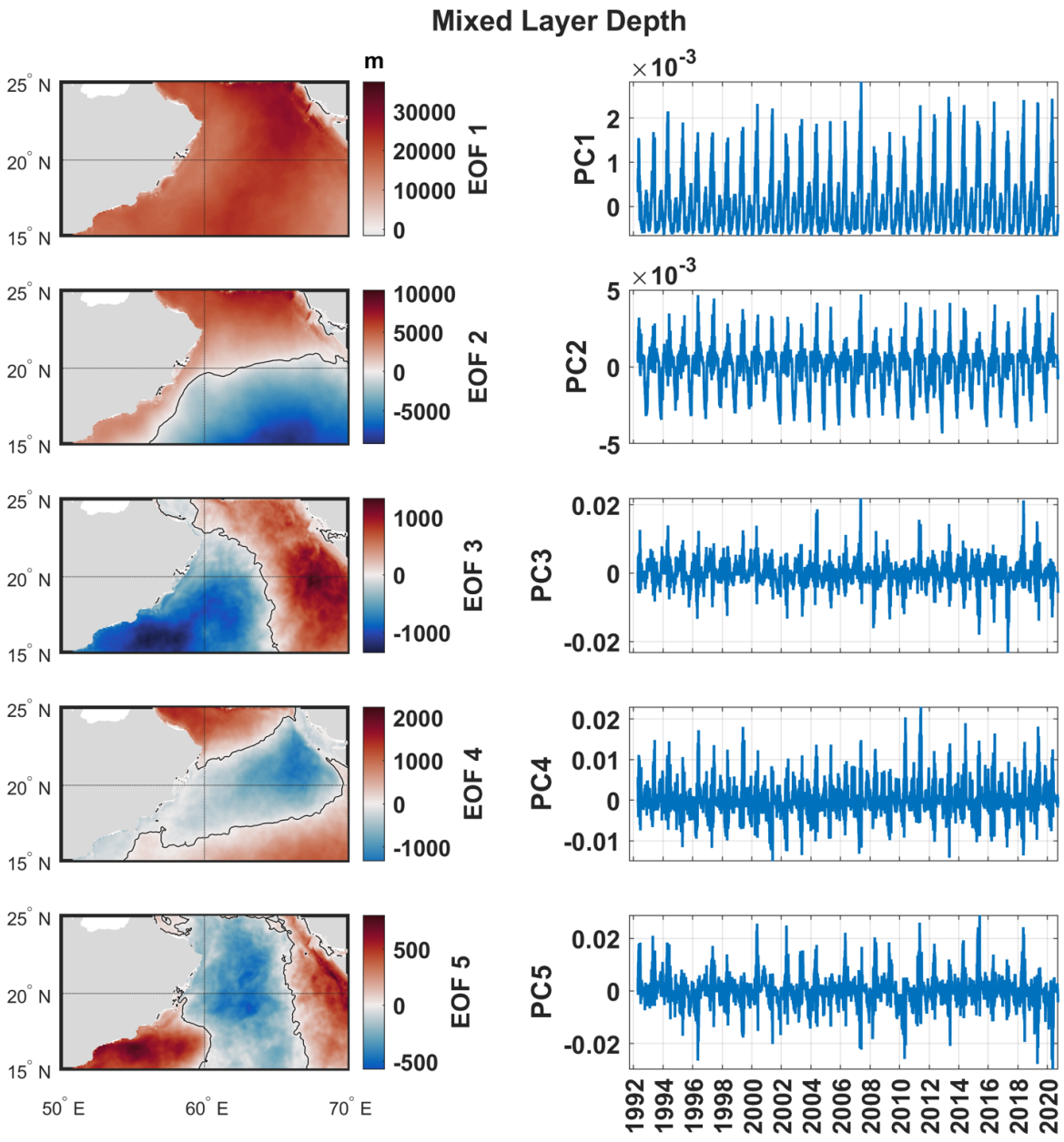

Black line in the EOF plot represents the zero contour.

Figure 14. EOF analysis of the MLD for 1993–2020

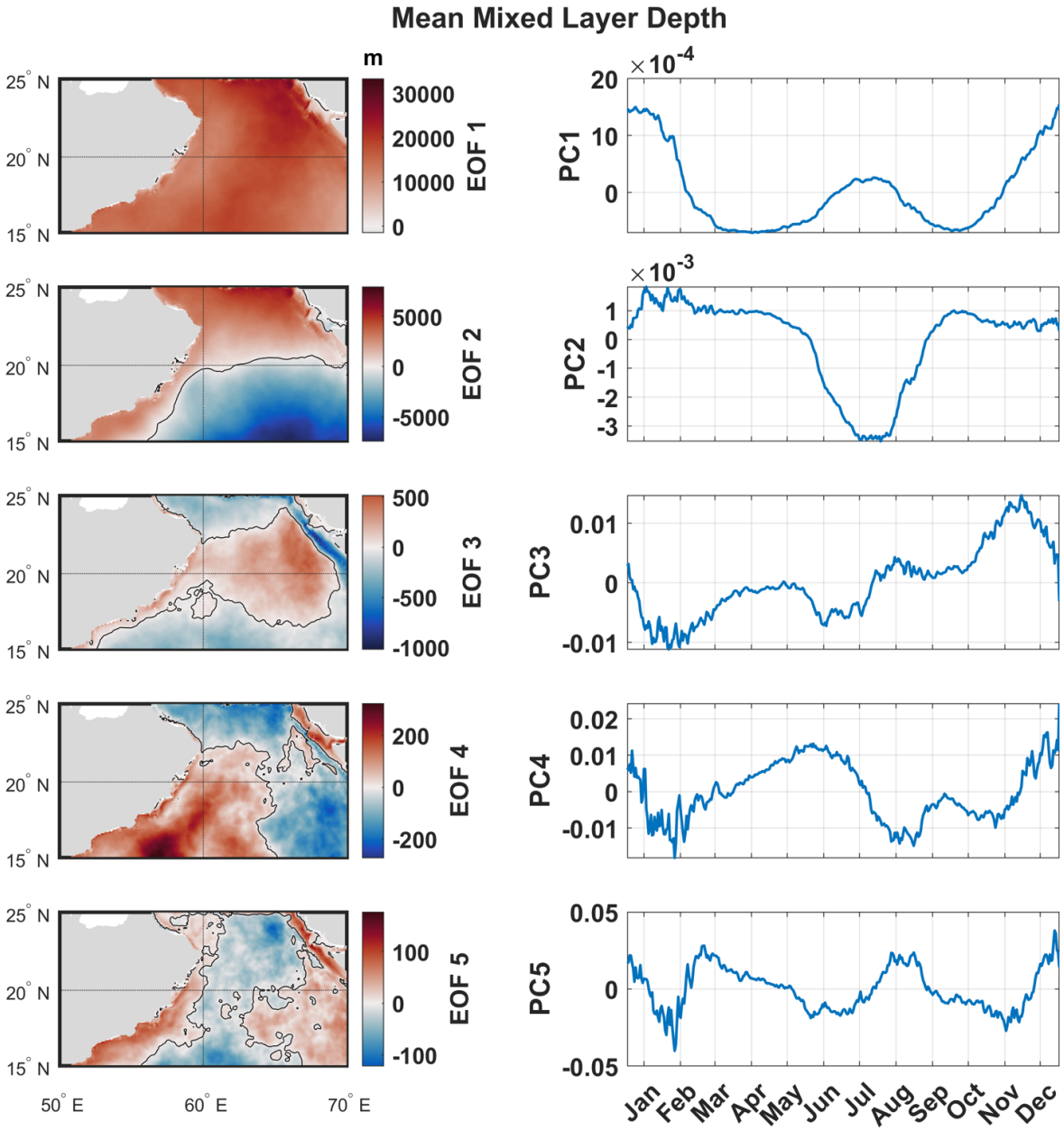

Black line in the EOF plot represents the zero contour.

Figure 15. EOF analysis of the MLD mean for 1993–2020

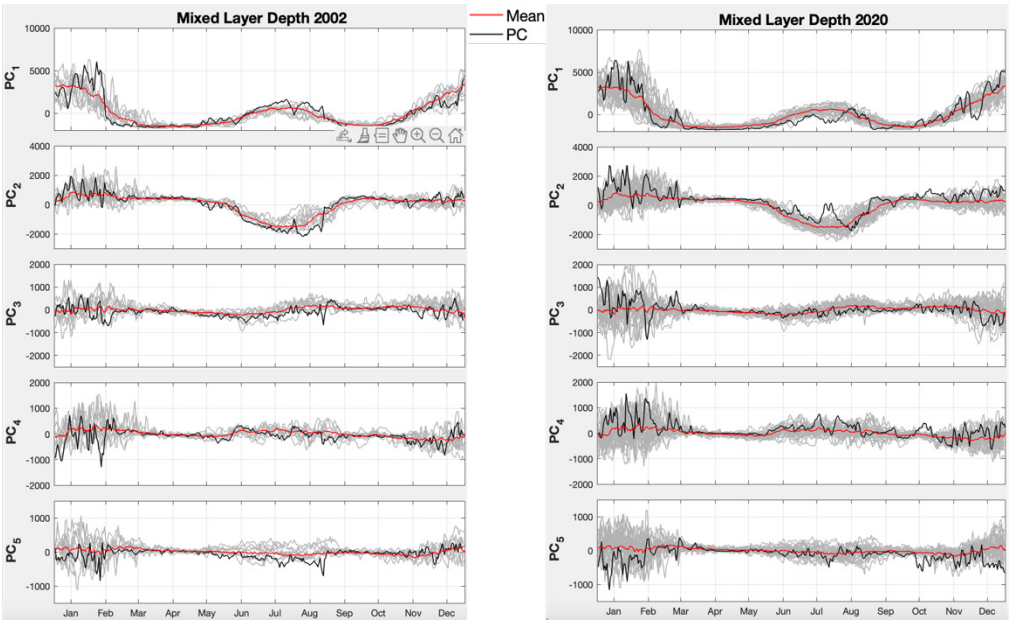

Red line depicts the mean for all years, black line is the PC value for the year listed, and the gray lines are previous years.

Figure 16. Interannual variability of PC for MLD in 2002 (left) and 2020 (right)

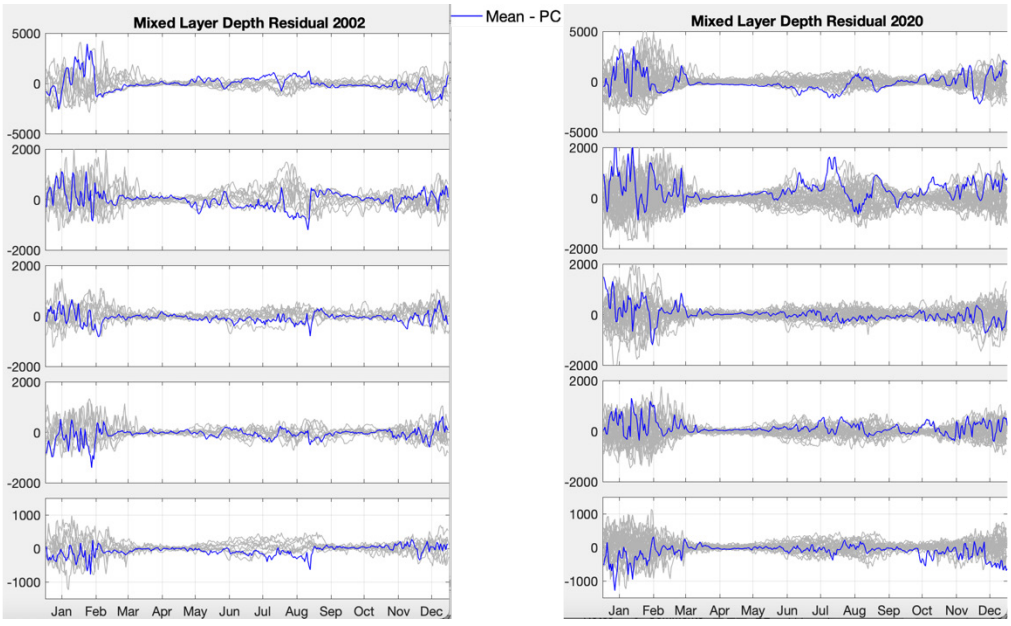

Blue line is difference by subtracting the year's actual PC value from the mean. This allows visualization of the difference of that year from the mean. Gray lines represent previous years. .

Figure 17. Interannual variability of PC for MLD residual in 2002 (left) and 2020 (right)

Figure 18 depict temperature's EOFs and their associated PCs. Figure 19 shows EOFs and their associated PCs for long term mean temperature. Focusing on the first two modes as they account for over 93% of the total variance, EOF1 shows two peaks on a yearly scale (see Figure 18) which indicates an ocean heat gain. The first peak (see Figure 19) occurs at the end of May aligning with the onset of the southwest monsoon and the second peak occurs in October during the transition season. This second peak can be a result of the horizontal advection from the southwest monsoon season. Overall, EOF1 is positive throughout with some localized neutrality along Oman's coast because of the upwelling. Ocean heat gain is strongest along the coastlines in the GOO.

The spatial pattern of EOF2 exhibits two varying zonal patterns (see Figure 18), with positive ocean heat gain occurring in the GOO and ocean heat loss occurring in the AS. EOF2 shows a distinct peak in August and a trough in mid-April (see Figure 19). This maxima in August are driven by the southwest monsoon as the cold water in the AS is advected northward. The minima are a result of the overall ocean heat loss that occurs during the northeast monsoon.

To better analyze the years 2002 and 2020, Figures 20 and 21 depict little similarities between the two-bloom occurring years. While PC3 in 2020 has a high residual value and PC1 had a weak residual value in the summer months, when the bloom was already diminishing. However, this may be one indication of why the bloom diminished. If water temperatures become too unfavorable, whether hot or cold, jellyfish are unable to continue reproducing in mass numbers.

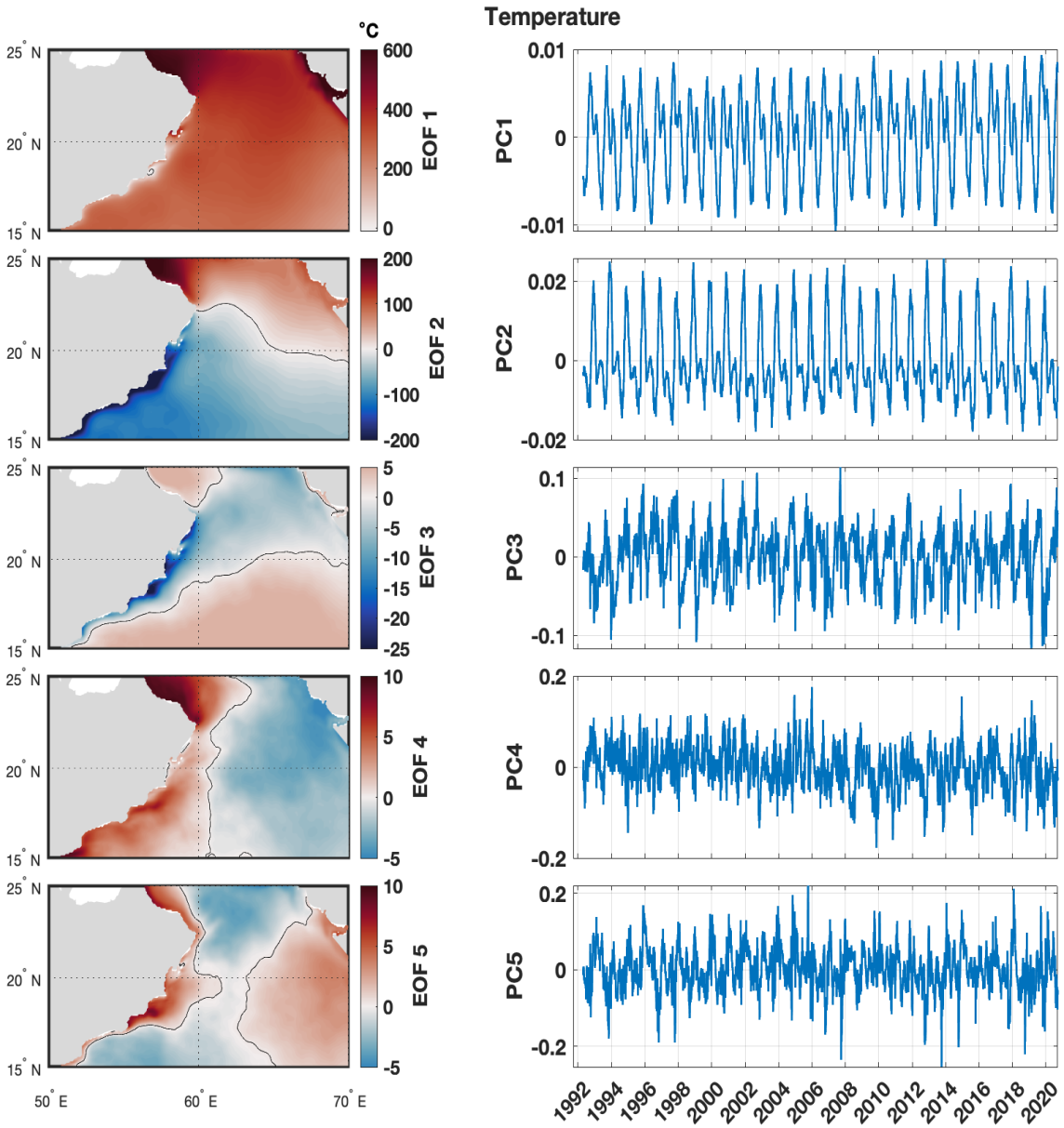

Black line in the EOF plot represents the zero contour.

Figure 18. EOF analysis of the temperature for 1993–2020

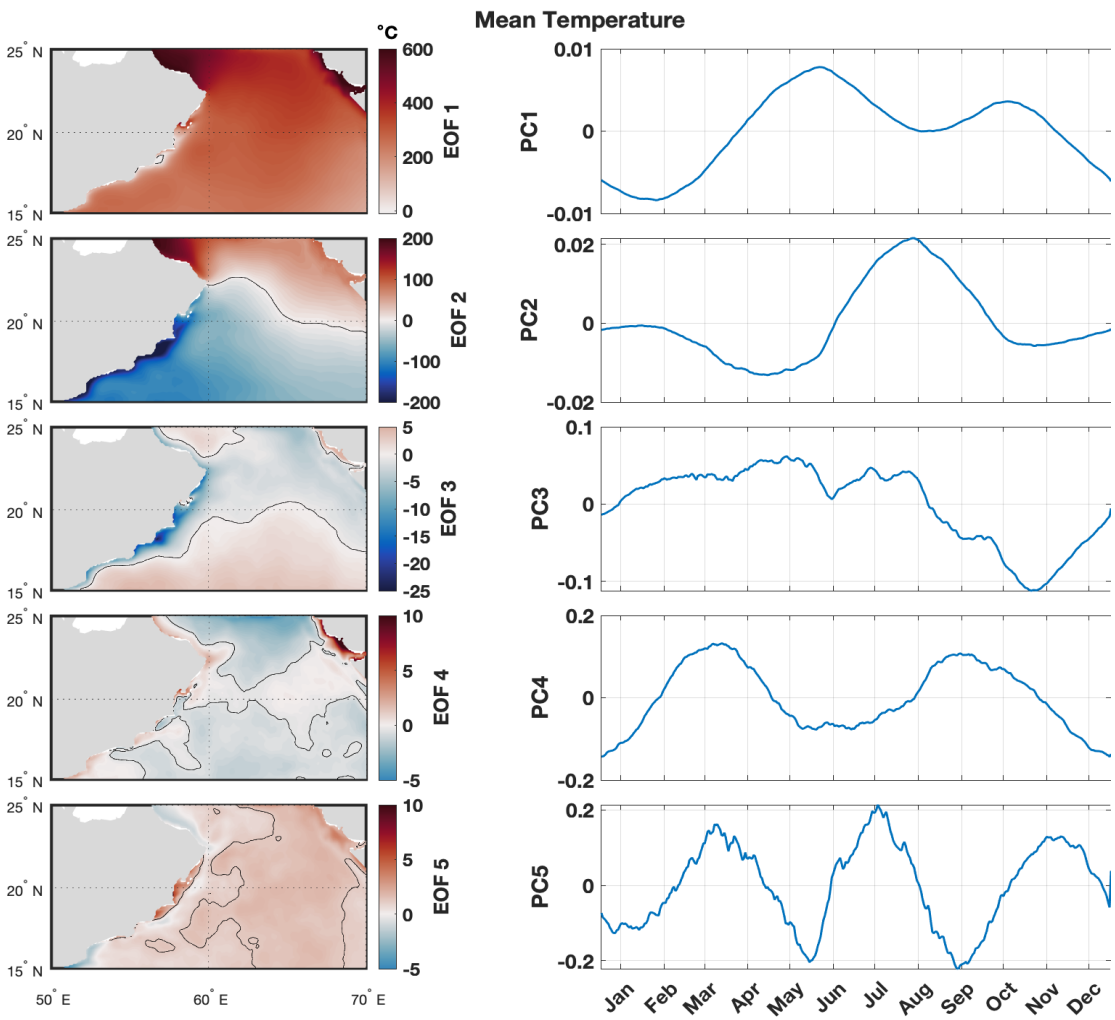

Black line in the EOF plot represents the zero contour.

Figure 19. EOF analysis of the temperature mean for 1993–2020

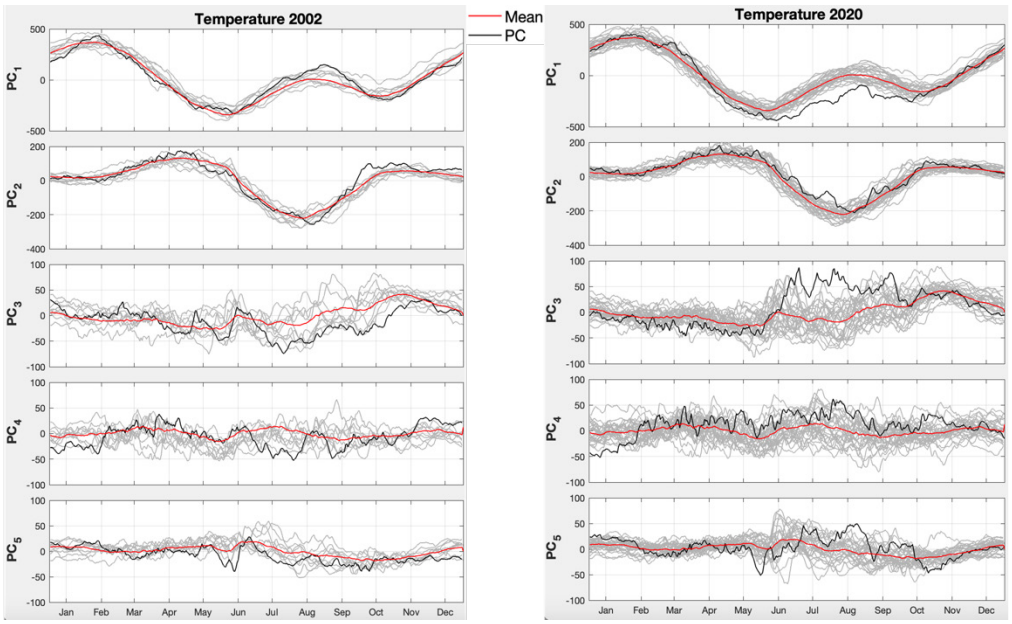

Red line depicts the mean for all years, black line is the PC value for the year listed, and the gray lines are previous years.

Figure 20. Interannual variability of PC for temperature in 2002 (left) and 2020 (right)

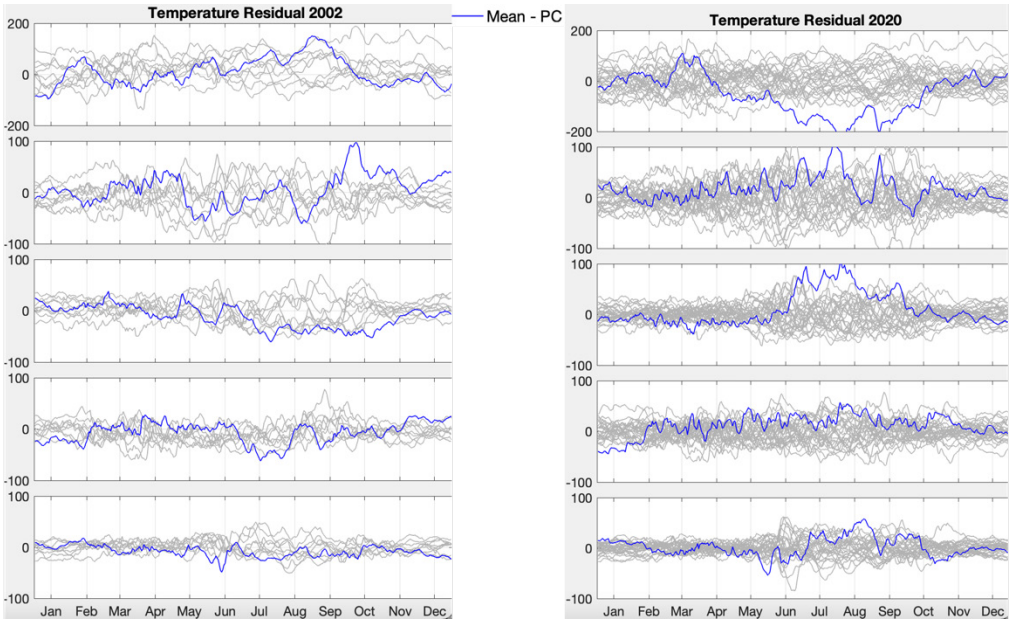

Blue line is difference by subtracting the year's PC value from the mean. This allows visualization of the difference of that year from the mean. Gray lines represent previous years.

Figure 21. Interannual variability of PC for temperature residual in 2002 (left) and 2020 (right)

D. CORRELATIONS

Ekman transport values were used to understand how each of the oceanographic parameters: chlorophyll-a, mixed layer depth, and temperature are affected by ET. By using the PCs for each of the three variables and the mean ET for that year we can assess potential relationship between two variables. Using the three different coastlines as displayed in Figure 3 and correlating it to the five PCs, the correlation coefficient is then calculated between the three coastlines' ET value and each of the five respective PCs. The associated lag time is also calculated alongside the correlation coefficient. The correlation coefficient ranges between -1 and +1 with its sign corresponding to the direction of the relationship between the two variables. A negative correlation coefficient value indicates that as one value increases the other variable decreases. The closer the correlation coefficient is to zero equates to a weaker relationship between the two variables.. In understanding this correlation, we are concerned with correlation coefficient values greater or less than +/- 0.50. This is known as Pearson's Linear Correlations Coefficient.

Only the tables (see Table 2 and 3) for coastlines #1 and #3 (see Figure 3) are shown as there was no significant values for coastline #2. The no significant values for coastline #2 indicates there is a lot of randomness between the two variables. Tables 2 and 3 depict the lag time associated between the two variables. For chlorophyll, MLD, and temperature driven by ET there is no pattern in the lag time. All values that are significant are highlighted in red. For coast #1, there is a strong relationship between ET and each of the three variables but vary in which PC. When comparing 2002 and 2020, the values are not unusual compared to other years.

Table 3 is for coast #3. There is no relationship between each of the variables for almost all years except 2019. In the year preceding the 2020 bloom, there is a moderate relationship between ET, chlorophyll, and MLD. Since the bloom began in February 2020 and originated off Pakistan's coast, it is likely that conditions in 2019 could be more substantial in affecting the 2020 bloom. This revelation could be one explanation for the bloom.

Table 4 displays how CHL-A and temperature are correlated to MLD. This table is not specific to a coastline but rather the entire region. The lag times for PC 1 and 2 are also of the same magnitude for each year. When comparing 2002 and 2020, one needs to look at the preceding and succeeding years. In the case of the 2002 bloom, it occurred later in the year, therefore, 2003's temperture values indicate a strong relationship in all PCs, except PC5. 2020 is the only other year this phenomenon occurred. Since 2020s bloom began in February and concluded in June, 2020s data is more relevant in understanding the ocean environment in which the bloom occurred.

Table 2. Correlation coefficients for CHL-A, MLD, and TEMP driven by ET annually from 1993 to 2020 for coast #1

CHL-A driven by ET: coast #1										
Years	PC_1	Lag	PC_2	Lag	PC_3	Lag	PC_4	Lag	PC_5	Lag
1993	-0.84	16	-0.51	24	0.15	30	-0.21	26	-0.61	0
1994	-0.81	22	0.59	5	0.25	21	-0.42	27	0.55	30
1995	-0.78	27	0.33	4	-0.33	11	-0.24	1	0.24	30
1996	-0.80	26	-0.41	30	0.23	30	-0.41	30	-0.79	1
1997	-0.76	30	0.48	12	-0.18	30	-0.40	18	0.56	30
1998	-0.76	30	-0.57	28	0.18	30	-0.23	30	-0.65	2
1999	-0.83	23	0.45	6	0.22	26	-0.44	1	-0.41	8
2000	-0.69	12	0.31	3	-0.31	0	-0.07	8	-0.32	13
2001	-0.73	14	0.19	17	-0.23	14	-0.18	30	-0.58	4
2002	-0.81	18	-0.44	30	0.23	30	-0.12	16	-0.75	2
2003	-0.69	20	-0.14	30	-0.35	13	0.15	30	-0.57	2
2004	-0.73	17	-0.28	26	-0.42	10	-0.13	0	0.16	12
2005	-0.73	10	-0.20	30	-0.26	13	0.23	12	-0.63	8
2006	-0.71	19	-0.26	30	-0.10	10	-0.43	19	0.21	25
2007	-0.65	30	-0.22	30	-0.57	23	0.26	23	-0.24	1
2008	-0.76	10	-0.19	30	-0.43	18	-0.17	29	-0.17	11
2009	-0.75	22	0.52	5	-0.57	30	-0.21	1	0.64	26
2010	-0.64	10	0.34	6	-0.57	25	0.30	24	0.28	30
2011	-0.72	29	0.31	7	-0.38	13	0.16	13	0.18	30
2012	-0.75	21	-0.33	1	-0.38	30	0.08	8	-0.24	0
2013	-0.77	18	0.27	0	-0.41	0	-0.13	25	0.52	18
2014	-0.70	14	-0.18	30	-0.14	11	-0.38	29	-0.24	0
2015	-0.68	25	-0.29	30	-0.57	28	0.39	11	-0.57	6
2016	-0.78	8	-0.36	30	-0.46	0	-0.22	30	0.43	19
2017	-0.74	21	0.42	0	-0.58	3	0.19	5	0.52	19
2018	-0.80	21	0.28	4	-0.20	4	-0.21	26	-0.30	0
2019	-0.79	30	-0.71	29	-0.10	20	0.34	12	-0.34	0
2020	-0.65	4	-0.21	29	-0.61	12	0.33	9	0.52	2

MLD driven by ET: coast #1										
Years	PC_1	Lag	PC_2	Lag	PC_3	Lag	PC_4	Lag	PC_5	Lag
1993	-0.12	16	-0.84	0	-0.34	3	0.40	29	-0.47	22
1994	-0.25	30	-0.75	0	0.16	26	-0.06	28	-0.16	28
1995	-0.33	0	-0.68	28	-0.31	4	0.11	1	-0.22	7
1996	-0.23	0	-0.79	0	-0.39	1	0.23	24	-0.09	4
1997	-0.30	0	-0.69	10	-0.16	11	0.12	1	0.37	10
1998	-0.31	0	-0.67	30	0.13	13	0.25	17	-0.31	18
1999	-0.19	0	-0.79	0	0.08	30	0.30	13	0.19	0
2000	-0.31	27	-0.70	0	-0.27	2	-0.23	9	-0.15	26
2001	-0.38	0	-0.69	14	0.11	30	0.39	21	0.24	29
2002	-0.09	0	-0.86	0	-0.27	2	0.24	1	-0.51	10
2003	-0.37	0	-0.64	0	0.14	25	0.36	2	-0.44	25
2004	-0.11	24	-0.71	0	0.36	30	-0.10	20	-0.72	18
2005	-0.30	22	-0.63	0	-0.35	2	0.34	1	-0.34	11
2006	-0.26	0	-0.71	0	0.12	22	0.15	22	-0.36	27
2007	-0.37	0	-0.62	0	-0.27	12	0.47	2	0.18	23
2008	-0.38	0	-0.73	0	0.26	30	0.23	4	-0.20	30
2009	-0.28	8	-0.74	0	-0.18	22	0.31	30	-0.23	0
2010	-0.36	0	-0.68	0	0.41	0	0.46	5	-0.37	29
2011	-0.15	0	-0.72	0	0.24	30	-0.07	11	-0.12	30
2012	-0.38	0	-0.61	16	-0.46	4	-0.23	15	-0.40	4
2013	-0.30	0	-0.67	0	0.15	25	0.34	6	-0.33	27
2014	-0.35	0	-0.71	0	0.13	24	-0.09	30	-0.44	10
2015	-0.39	0	-0.62	19	0.48	19	0.22	2	-0.33	30
2016	-0.20	0	-0.75	0	0.38	30	0.28	18	-0.26	25
2017	-0.39	0	-0.67	14	0.49	19	0.39	17	0.13	0
2018	0.06	17	-0.78	1	0.11	14	0.36	5	-0.42	13
2019	-0.31	20	-0.78	7	-0.31	9	0.21	9	0.08	30
2020	-0.49	0	-0.70	0	-0.12	7	-0.09	18	0.36	0

TEMP driven by ET: coast #1										
Years	PC_1	Lag	PC_2	Lag	PC_3	Lag	PC_4	Lag	PC_5	Lag
1993	-0.55	0	-0.77	26	0.28	30	-0.65	13	-0.26	30
1994	-0.36	0	-0.74	25	-0.43	0	-0.39	25	0.59	2
1995	-0.54	0	-0.69	30	-0.67	1	0.38	30	-0.28	26
1996	-0.56	0	-0.72	30	-0.64	8	-0.38	18	-0.55	30
1997	-0.53	0	-0.70	28	-0.21	1	0.22	29	0.68	2
1998	-0.55	0	-0.68	30	-0.61	2	0.33	5	0.29	1
1999	-0.48	0	-0.80	30	-0.68	2	0.43	30	-0.30	30
2000	-0.41	0	-0.75	16	-0.63	7	-0.23	0	-0.51	29
2001	-0.46	0	-0.67	26	-0.52	2	-0.35	0	-0.23	30
2002	-0.37	0	-0.74	27	-0.71	8	-0.53	27	-0.40	24
2003	-0.55	0	-0.65	29	0.15	30	0.48	9	0.40	1
2004	-0.41	0	-0.65	24	-0.41	14	-0.27	16	-0.44	27
2005	-0.43	0	-0.59	30	-0.65	2	0.15	4	-0.65	24
2006	-0.46	0	-0.64	27	-0.40	2	-0.46	30	0.11	26
2007	-0.47	0	-0.55	30	0.17	24	0.14	22	0.31	1
2008	-0.50	0	-0.66	11	-0.23	2	-0.11	30	0.46	1
2009	-0.54	0	-0.71	26	0.30	30	-0.55	19	0.58	1
2010	-0.51	0	-0.52	30	0.28	30	0.65	5	-0.14	28
2011	-0.45	0	-0.66	30	-0.50	1	0.19	23	0.34	1
2012	-0.48	0	-0.69	30	-0.53	0	-0.11	28	-0.44	13
2013	-0.41	0	-0.67	14	0.15	10	0.52	2	0.48	2
2014	-0.44	0	-0.63	19	-0.24	10	0.49	9	0.35	0
2015	-0.37	1	-0.54	22	-0.31	17	-0.53	30	0.24	1
2016	-0.49	0	-0.66	30	-0.25	4	-0.26	30	0.29	1
2017	-0.51	0	-0.66	30	-0.20	2	-0.20	23	-0.30	24
2018	-0.30	0	-0.72	27	-0.65	1	-0.43	30	0.46	2
2019	-0.46	0	-0.69	30	-0.46	2	0.65	9	-0.24	19
2020	-0.60	29	-0.50	5	0.50	30	0.49	2	0.46	3

Significant PC correlation coefficient values are highlighted in red. Associated lag times in days for each PC is highlighted in blue.

Table 3. Correlation coefficients for CHL-A, MLD, and TEMP driven by ET annually from 1993 to 2020 for coast #3

CHL-A driven by ET: coast #3											MLD driven by ET: coast #3										TEMP driven by ET: coast #3									
Years	PC_1	Lag	PC_2	Lag	PC_3	Lag	PC_4	Lag	PC_5	Lag	Years	PC_1	Lag	PC_2	Lag	PC_3	Lag	PC_4	Lag	PC_5	Lag	Years	PC_1	Lag	PC_2	Lag	PC_3	Lag	PC_4	Lag	PC_5	Lag
1993	-0.17	0	-0.17	4	-0.18	30	-0.24	13	-0.18	30	1993	-0.33	30	-0.22	5	-0.28	20	0.25	30	-0.32	21	1993	-0.39	30	-0.08	18	-0.26	1	-0.33	5	0.20	7
1994	-0.17	30	0.14	12	0.11	3	-0.22	4	0.11	9	1994	-0.27	30	-0.21	3	-0.17	27	-0.12	29	-0.16	1	1994	-0.30	30	-0.12	30	-0.45	2	-0.16	23	0.24	9
1995	-0.28	5	0.06	0	-0.36	30	-0.22	2	0.22	30	1995	-0.31	26	-0.27	28	-0.27	20	0.13	30	-0.19	7	1995	-0.34	30	-0.20	29	-0.44	9	0.10	30	-0.10	30
1996	-0.36	30	-0.21	30	-0.14	0	-0.29	9	-0.43	3	1996	-0.23	16	-0.36	6	-0.24	14	0.20	17	0.11	15	1996	-0.42	18	-0.26	29	-0.50	3	-0.29	6	-0.12	30
1997	-0.19	30	0.23	13	-0.19	30	-0.19	18	0.16	29	1997	-0.29	26	-0.23	25	-0.31	25	0.20	28	0.22	12	1997	-0.27	29	-0.15	30	-0.38	2	0.13	28	0.33	25
1998	-0.38	30	-0.32	19	0.14	3	-0.14	23	-0.31	3	1998	-0.29	18	-0.32	24	0.15	1	0.31	0	-0.09	1	1998	-0.30	30	-0.25	30	-0.53	1	0.19	30	0.10	4
1999	-0.38	25	0.27	7	0.15	20	-0.32	20	-0.24	3	1999	-0.11	5	-0.41	15	-0.11	18	0.20	8	0.23	5	1999	-0.24	8	-0.35	30	-0.45	2	0.11	0	0.06	11
2000	-0.36	30	0.19	30	-0.24	30	-0.14	3	-0.22	19	2000	-0.22	9	-0.38	26	-0.20	14	-0.20	14	0.11	27	2000	-0.27	0	-0.38	26	-0.37	9	-0.23	2	-0.19	30
2001	-0.33	14	0.19	19	-0.18	0	-0.20	30	-0.44	8	2001	-0.22	21	-0.33	14	-0.13	23	0.30	15	0.11	30	2001	-0.24	29	-0.29	30	-0.45	4	-0.28	6	0.08	0
2002	-0.31	29	-0.10	13	-0.15	0	-0.10	13	-0.36	16	2002	-0.12	21	-0.40	28	-0.25	20	0.20	30	-0.30	15	2002	-0.27	21	-0.32	30	-0.49	13	-0.29	9	-0.18	22
2003	-0.24	13	-0.11	28	-0.32	30	-0.13	26	-0.30	2	2003	-0.27	20	-0.24	16	-0.10	16	0.12	1	-0.24	11	2003	-0.38	30	-0.19	30	-0.29	1	0.14	0	0.18	4
2004	-0.42	22	-0.16	21	-0.28	11	-0.16	2	-0.25	3	2004	-0.14	9	-0.40	2	0.19	2	0.15	10	-0.44	19	2004	-0.32	13	-0.36	30	-0.36	3	-0.13	5	-0.16	19
2005	-0.26	6	-0.08	7	-0.21	30	-0.13	24	-0.24	30	2005	-0.25	12	-0.25	23	-0.30	12	0.19	0	-0.24	14	2005	-0.25	29	-0.18	28	-0.34	1	0.13	0	-0.21	14
2006	-0.33	8	-0.17	30	0.07	3	-0.28	2	-0.29	2	2006	-0.23	13	-0.34	22	-0.13	2	-0.13	2	-0.23	28	2006	-0.32	28	-0.28	30	-0.50	2	-0.34	30	-0.19	12
2007	-0.25	5	-0.28	24	-0.31	26	0.13	26	-0.24	3	2007	-0.32	14	-0.08	4	-0.19	15	0.10	14	0.10	10	2007	-0.26	30	-0.10	2	-0.32	5	-0.16	19	-0.23	16
2008	-0.34	3	-0.15	28	-0.25	30	-0.14	7	-0.19	15	2008	-0.30	14	-0.33	3	0.07	30	0.13	0	0.11	16	2008	-0.33	26	-0.24	30	-0.40	3	-0.21	10	0.16	30
2009	-0.31	30	0.28	0	-0.41	30	-0.19	17	0.32	6	2009	-0.34	17	-0.37	7	-0.24	26	0.16	30	-0.25	2	2009	-0.43	30	-0.27	30	-0.11	1	-0.32	21	0.29	8
2010	-0.17	30	0.14	20	-0.32	30	0.10	30	-0.14	30	2010	-0.30	5	-0.28	30	0.29	10	0.23	20	-0.13	30	2010	-0.41	24	-0.07	30	-0.34	1	0.31	12	-0.18	23
2011	-0.34	30	0.22	8	-0.36	8	0.14	9	-0.18	2	2011	-0.21	6	-0.42	30	-0.14	29	-0.14	13	0.15	0	2011	-0.41	24	-0.27	30	-0.41	2	0.06	8	0.17	9
2012	-0.42	20	-0.14	30	-0.23	27	0.12	0	-0.17	2	2012	-0.28	25	-0.34	24	-0.32	18	-0.15	24	-0.29	1	2012	-0.28	27	-0.35	30	-0.48	4	-0.18	4	-0.28	1
2013	-0.16	2	-0.13	17	-0.28	30	-0.23	17	0.21	10	2013	-0.34	7	-0.17	27	-0.20	18	0.24	19	-0.13	17	2013	-0.39	30	-0.10	30	-0.31	1	0.22	21	0.14	30
2014	-0.32	16	-0.08	13	-0.14	0	-0.21	26	-0.29	7	2014	-0.20	12	-0.36	19	-0.17	7	-0.12	30	-0.34	5	2014	-0.26	13	-0.28	25	-0.35	5	0.28	17	0.24	22
2015	-0.38	27	-0.38	28	-0.39	13	0.32	14	-0.46	4	2015	-0.19	7	-0.32	21	0.27	1	0.12	12	-0.22	29	2015	-0.21	30	-0.26	4	-0.40	8	-0.31	30	-0.14	18
2016	-0.29	30	0.06	0	-0.41	21	0.18	21	-0.19	5	2016	-0.28	15	-0.37	28	0.23	16	0.18	19	-0.14	1	2016	-0.45	22	-0.18	30	-0.50	2	0.12	0	-0.20	1
2017	-0.38	22	0.25	0	-0.37	0	-0.14	30	0.26	18	2017	-0.32	13	-0.37	20	0.34	18	0.32	16	0.13	13	2017	-0.34	26	-0.24	24	-0.21	2	-0.26	24	-0.21	10
2018	-0.32	23	0.12	25	-0.21	5	-0.14	2	-0.16	2	2018	-0.22	11	-0.35	30	-0.08	30	0.22	10	-0.35	16	2018	-0.35	27	-0.26	30	-0.43	2	-0.09	11	0.21	5
2019	-0.49	5	-0.47	4	-0.22	30	0.10	0	0.28	30	2019	-0.29	30	-0.47	10	-0.16	13	0.10	14	0.10	30	2019	-0.28	30	-0.29	18	-0.36	3	0.49	2	-0.41	2
2020	-0.23	3	-0.12	18	-0.35	10	-0.12	24	0.21	30	2020	-0.41	8	-0.39	4	-0.15	19	-0.15	25	0.31	0	2020	-0.48	30	-0.10	30	0.21	30	0.32	12	0.07	10

Significant PC correlation coefficient values are highlighted in red. Associated lag times in days for each PC is highlighted in blue.

Table 4. Correlation coefficients for CHL-A and TEMP driven by MLD annually from 1993 to 2020 for the study region

CHL-A driven by MLD											TEMP driven by MLD										
Years	PC_1	Lag	PC_2	Lag	PC_3	Lag	PC_4	Lag	PC_5	Lag	Years	PC_1	Lag	PC_2	Lag	PC_3	Lag	PC_4	Lag	PC_5	Lag
1993	0.68	28	0.49	30	0.76	6	0.50	3	0.44	17	1993	0.71	6	0.78	28	-0.56	30	0.46	5	0.39	30
1994	0.71	29	-0.48	23	0.67	6	0.26	3	-0.45	30	1994	0.80	7	0.80	28	-0.38	26	0.54	9	-0.35	11
1995	0.58	28	0.25	1	0.73	7	0.47	3	0.28	8	1995	0.78	7	0.76	29	0.38	0	-0.47	24	0.39	30
1996	0.71	29	0.42	30	0.67	7	0.43	0	0.52	25	1996	0.74	7	0.79	29	0.34	22	0.32	16	0.64	30
1997	0.70	30	-0.39	20	0.71	5	0.49	10	-0.57	30	1997	0.79	8	0.81	29	-0.37	18	-0.49	30	-0.62	18
1998	0.64	27	0.47	30	0.66	7	0.42	3	0.43	18	1998	0.80	7	0.83	28	0.16	19	-0.42	16	0.33	0
1999	0.69	28	-0.44	19	0.62	5	0.25	4	0.36	15	1999	0.76	7	0.79	29	0.32	27	-0.66	30	0.58	30
2000	0.62	29	-0.21	21	0.75	8	0.67	7	0.22	5	2000	0.85	6	0.63	26	0.38	29	-0.64	27	0.61	30
2001	0.59	29	-0.26	18	0.76	6	0.52	4	0.32	6	2001	0.88	8	0.67	27	-0.47	27	-0.42	30	0.46	30
2002	0.68	30	0.27	0	0.68	6	0.48	4	0.44	25	2002	0.80	6	0.68	27	0.28	30	0.37	30	0.39	0
2003	0.66	29	-0.28	14	0.78	7	0.79	7	0.49	24	2003	0.76	7	0.80	29	-0.53	29	-0.55	30	0.37	4
2004	0.66	30	-0.26	17	0.62	5	0.51	5	0.23	4	2004	0.76	6	0.80	29	-0.36	4	0.39	10	0.49	30
2005	0.66	30	-0.35	13	0.73	5	0.57	8	0.36	28	2005	0.74	6	0.81	29	0.26	18	-0.22	12	0.40	30
2006	0.54	30	0.31	0	0.81	7	0.40	3	0.31	16	2006	0.73	7	0.64	30	0.16	19	0.36	0	0.28	0
2007	0.52	28	-0.26	16	0.61	6	0.52	5	0.16	15	2007	0.72	6	0.66	30	-0.38	10	-0.58	30	0.42	0
2008	0.53	29	0.26	0	0.76	6	0.61	5	-0.30	30	2008	0.81	8	0.72	28	-0.50	28	-0.25	24	0.19	30
2009	0.69	30	-0.37	19	0.64	4	0.49	7	-0.56	30	2009	0.80	8	0.77	28	-0.27	30	0.62	16	-0.49	14
2010	0.70	30	-0.37	20	0.47	4	-0.59	28	-0.39	30	2010	0.79	6	0.83	30	-0.46	27	-0.30	25	0.30	23
2011	0.78	30	-0.38	24	0.62	7	0.44	3	0.32	16	2011	0.78	8	0.89	28	-0.18	6	-0.45	27	0.29	0
2012	0.61	27	0.23	26	0.76	5	0.63	7	-0.41	30	2012	0.88	7	0.75	28	-0.25	30	-0.27	5	0.31	26
2013	0.66	30	-0.33	16	0.71	6	0.42	5	-0.52	30	2013	0.83	7	0.78	28	-0.55	19	-0.29	21	-0.42	15
2014	0.55	28	0.25	1	0.76	9	0.62	4	0.36	11	2014	0.80	9	0.67	28	-0.38	24	-0.31	3	0.40	30
2015	0.54	30	0.23	0	0.58	4	-0.53	29	0.33	25	2015	0.82	8	0.65	25	-0.28	11	0.48	27	0.37	29
2016	0.71	29	-0.27	16	0.54	7	0.38	2	-0.58	30	2016	0.76	6	0.87	30	-0.38	30	0.26	19	-0.38	16
2017	0.59	30	-0.27	16	0.65	4	-0.51	26	-0.36	29	2017	0.82	6	0.76	27	-0.36	26	0.53	6	0.39	30
2018	0.78	30	-0.32	20	0.74	6	0.39	4	0.31	17	2018	0.78	7	0.88	29	0.35	29	-0.47	6	0.39	0
2019	0.61	27	0.47	30	0.67	4	0.59	4	0.29	14	2019	0.81	7	0.80	28	-0.25	30	-0.33	30	0.18	11
2020	0.50	30	-0.15	12	0.61	3	-0.53	30	-0.50	30	2020	0.77	8	0.74	28	-0.84	30	-0.61	1	-0.34	29

Significant PC correlation coefficient values are highlighted in red. Associated lag times in days for each PC is highlighted in blue.

THIS PAGE INTENTIONALLY LEFT BLANK

V. DISCUSSION

As the results indicate, there is no one uniform cause of the *c. orsini* bloom between 2002 and 2020 and it is difficult to quantify a numerical threshold for bloom prediction especially as the timeframes, temporal scales, and locations vary between years. However, the results do indicate that a multilayered approach must be taken to understand why the bloom occurred. Bloom favorable conditions are determined by monsoonal winds, elevated primary productivity, and moderate water temperature which serves as a limiting factor. Monsoonal winds drive the upwelling by causing the offshore ET and provide advective transport into more favorable temperate waters as seen in temperature's EOF1 (see Figure 19). Where the bloom originates and where the jellyfish become problematic to naval operations or local fisherman are different areas (see Figure 3). Next, primary production via an abundance of chlorophyll-a correlating to the production of mixed diatom blooms. As mentioned in the introduction, mixed diatom blooms are eaten by the *n. scintillans* which, in turn, are eaten by the *c. orsini*. This is critical to understand as average SST serves as the limiting factor for the jellyfish. It is typically thought that jellyfish thrive in warmer waters. However, this is only the case when there is a food source available. As mentioned by Harrison et al. (2011), the green *n. scintillans* typically found in the northern AS, require a temperature range of 25°C-30°C to reproduce in large concentrations. As depicted in the results, the *c. orsini* cease to continue blooming when SST are too hot, as in 30°C or greater, and too cold, as in 25°C or less due to a lack of food source. The threshold that is uniform among the two years is temperature being driven by MLD (see Table 4) which is evidence of a change in the environment compared to the other 26 years of data. EOF2 in Figure 15 exhibits how the MLD spatial pattern of the GOO and AS shift with the onset/offset of the monsoon seasons lending support that strong vertical mixing could be one indication of a bloom. Table 4 further shows that 2003 (year following the 2002 bloom) and 2020 exhibited a higher correlation of SST and MLD in the four most dominant PCs.

EOF analysis clarifies the spatial and temporal scales of the main oceanographic processes of the region. EOF analysis provides the variability around the average state by

removing the seasonality and mean. Figure 10 is oriented based on the coasts, whereas Figures 14 and 18 depict the zonal and meridional signals across each of the modes. Modes 1 and 2 are zonal, mode 3 is meridional, and mode 4 and 5 vary between smaller scale zonal or meridional signals. Understanding the patterns in these signals provides recognition of the variability in the region. Alluded to previously, is the understanding that the AS circulations are driven by the monsoons thus making them strongly seasonal in nature (Talley et al. 2011). As seen in Figure 10, EOF1 corresponds to these seasonal variations in chlorophyll-a concentration as the upwelling is aligned with the summer monsoon. Also associated with the monsoon seasons, the ocean circulations also undergo a complete reversal with the stronger ocean circulations and wind flow associated with the southwest monsoon (Talley et al. 2011). During the southwest monsoon, the fast Somali Current contributes to the northward flow along Oman's coast. At the entrance to the GOO is the eastward jet called the Ras al Hadd Jet (Talley et al. 2011). Contrarily, during the northeast monsoon, the surface circulations in the AS reverse with the Somali current flowing southward and the West Indian Coastal Current flowing westward (Talley et al. 2011). As the overall ocean circulation is less consistent during the northeast monsoon, there is a higher likelihood for smaller scale variability in the AS and GOO region.

A. 2002 BLOOM

Figure 6 depicts the cooler water that is upwelling along the Iranian coast. When paired with Figure 8, it can be seen how ET fluctuates along the same coastline. As this bloom originates and is sustained through the summer monsoon season. Figure 2(b) depicts the southwest wind which causes ET to occur in the region and Figure 2(d) shows the currents that advect the upwelled water away from the coast. Figure 22 shows the sea surface height (SSH) and current velocity for August 8, 2002 providing a quick snapshot of the sea surface currents during the bloom and shows the Ras al Hadd Jet producing an anticyclonic eddy. It is evident in Figure 22 that the southwest wind induced upwelling in the region lends support for chlorophyll-a along Oman's coast (see Figure 4). These nutrients could be transported to the northeast along the jet providing sustenance for the *c. orsini;* although this was not mentioned in Daryanabard and Dawson's (2008) study. Lastly, SST are average for the region but become cooler in the AS and notably cooler in

the 2002b box (Figure 3) with the change of the monsoon season. In December 2002, cooler water temperature due to the monsoon season change curb the overproduction of *c. orsini.*

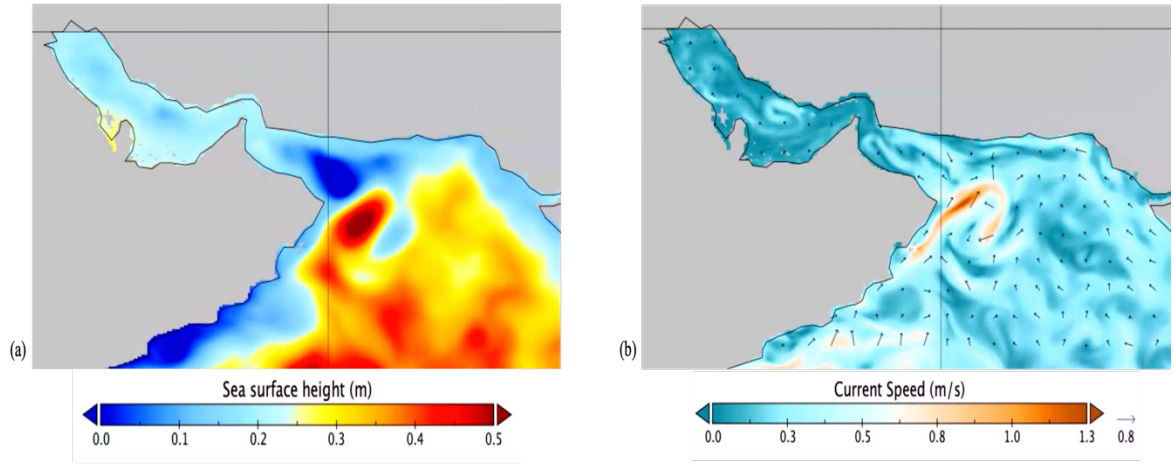

(a) SSH in meters. (b) Ocean current speed in m/s.

Figure 22. Ocean circulation patterns at 1200 UTC on August 8, 2002

B. 2020 BLOOM

Figure 7 depicts the cooler, water that is upwelling along the Pakistani coast when paired with Figure 9, it is apparent that there is strong upwelling in the region. As the bloom began in February 2020, during the winter monsoon season, Figure 2(a) depicts the northeast wind that can be a contributing factor in transporting the *c. orsini* away from Pakistan's coast and acts as a mixing mechanism in the region. Figure 23 shows the SSH and current velocity for February 12, 2020, which indicate there are two cyclonic eddies offshore of Oman enhancing the stirring in the region. Figure 23(b) illustrates the currents that transport the nutrient rich water and *c. orsini* away from Pakistan's coast towards Oman, where U.S. Navy ships were operating. While Figure 5 shows minimal chlorophyll-a concentration along the origination area, there are higher concentrations along the southeast Arabian Peninsula. The chlorophyll-a concentration in 2020 is not significant, as 2021 displayed more concentrated values. The bloom ended by June 2020, but it is unknown whether the 2020 bloom was one continuous event beginning in February or a series of multiple blooms. This thesis inferred it was one continuous bloom. Temperatures

for the region are average during the bloom. However, as the transition occurs to the summer monsoon, SSTs increase above 30°C during late May, lending an explanation as to why *c. orsini* ceased to bloom.

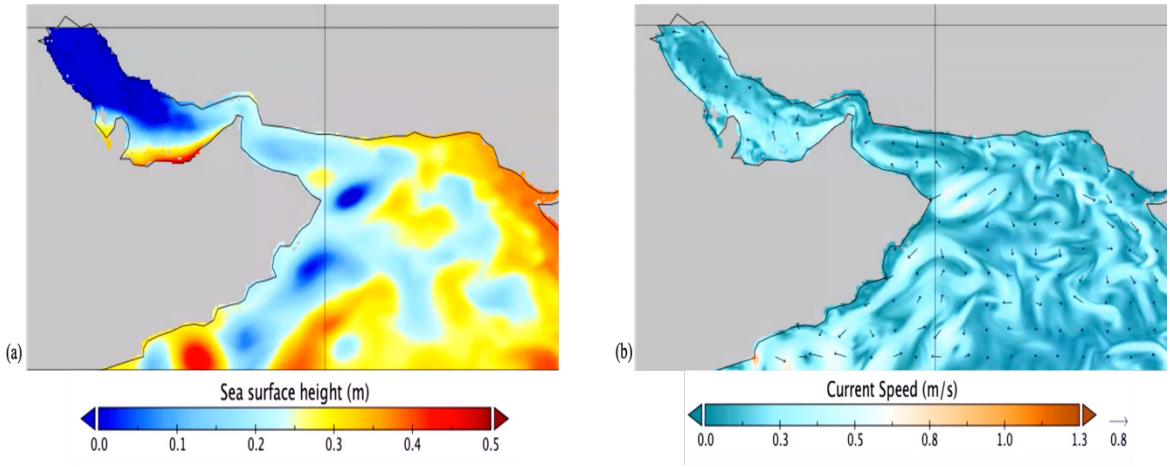

(a) SSH in meters. (b) Ocean current speed in m/s.

Figure 23. Ocean circulation patterns at 1200 UTC on February 12, 2020

C. CLIMATOLOGICAL INDICES

ENSO and Dipole Mode Index (DMI) were analyzed to see if there are any global patterns that are similar amongst 2002 and 2020. Figure 24 shows ENSO and Figure 25 shows DMI, which is an indication of the IOD phases, with the yellow dashed line highlighting the two years. The 2002 bloom occurred during an ENSO and DMI neutral year. Whereas, 2020s bloom occurred in a slightly positive, yet neutral ENSO year but a high DMI, which equates to a positive IOD. This positive IOD was the strongest of the century with significant effects on the SST and biological activity in the equatorial Indian Ocean, 10°S to 10°N (Shi and Wang 2021). While this area is south of the bloom region, the anomalous activity associated with the IOD may have affected *c. orsini* study region. While there are no similarities between the two years, understanding the uniqueness of 2019–2020s positive IOD could be another indication of favorable conditions for a *c. orsini* bloom. In 2019, the correlation between chlorophyll-a and ET is much higher than the median. Table 3's relatively high correlation coefficient in 2019, -.49 for PC1 and -.47 for

PC2 as compared to median -.32 and -.09 for each respective PC could be a result of this strong, positive IOD.

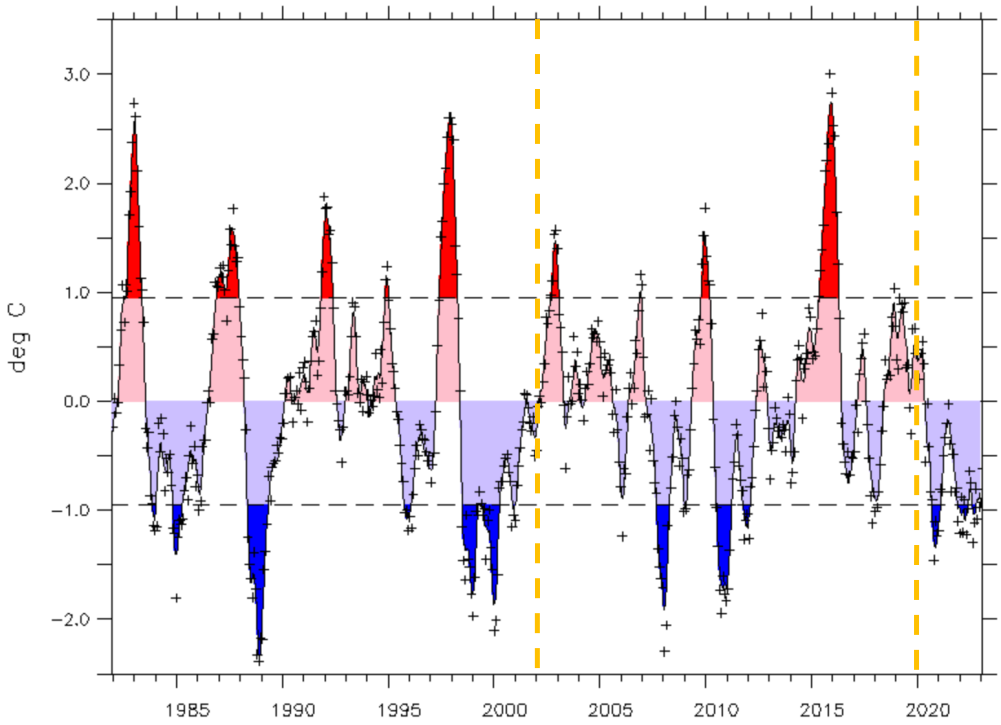

Yellow dashed line indicate years of interest: 2002 and 2020

Figure 24. ENSO 3.4 for 1982–2023. Source: NOAA/OSMC (2023b)

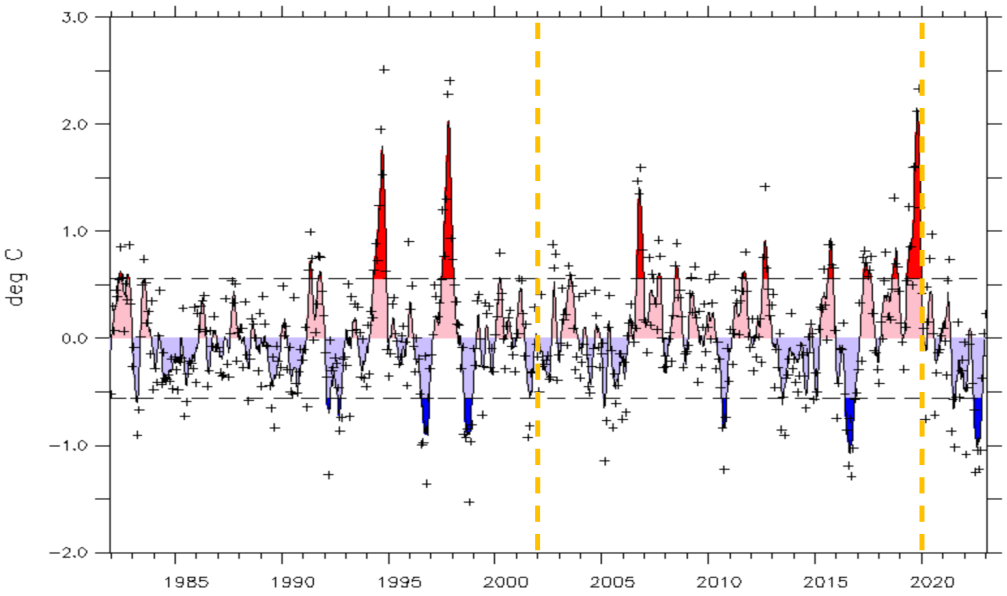

Figure 25. DMI for 1982–2023. Source: NOAA/OSMC (2023a)

VI. CONCLUSIONS AND FUTURE WORK

We hypothesized that the monsoon-driven enhanced upwelling and heightened convective mixed layer resulted in increased nutrient availability fueling the food chain from mixed diatoms to *n. scintillans* to *c. orsini.* The results are consistent with the hypothesis but the general understanding of what causes a *c. orsini* bloom was greatly expanded. We found that just having one of the following parameters/events: upwelling, chlorophyll concentration, SST, monsoonal winds/currents, or the jellyfish present is not enough to support a bloom event. It takes a combination of these different factors to produce a bloom. Originally, the objective of this thesis was to determine the main environmental drivers and limiting factors of the endemic *c. orsini* blooms in the AS and GOO and to facilitate their forecasts with at least a 1–2 day lead time by using easy-to-interpret oceanographic information. We found that to facilitate these forecasts, one must understand the aforementioned parameters/events and how they interact with each other. First, the *c. orsini* must be present in coastal waters where upwelled water can supply the jellyfish's food source, *n. scintillans,* with an overabundance of nutrients. Chlorophyll concentration is an indication of nutrient availability. SST must be average in the region, 25°C-30°C, to support survival of the *n. scintillans*. Lastly, monsoonal winds and currents are needed to induce advective transport to either more temperate waters or an area where there is a wealth of food available to support a bloom. The intricate combination of these parameters/events results in a *c. orsini* bloom, hence, why they occur so infrequently, on a greater than decadal scale. The main environmental driver of a *c. orsini* bloom is the monsoon season and the limiting factor is the SST.

While the two years that the blooms occurred have varying timeframes, temporal scales, and locations, the underlying cause, environmental driver, limiting factor, and geographic vastness remain the same. Both blooms originated with having c. *orsini* in coastal, upwelled water during the monsoon season which provide advective transport to an area with an abundant food source and favorable water. Both blooms concluded with a change in water temperature as their food source diminished. Understanding these similarities is critical in providing a forecast for when a bloom may occur.

Additionally, technology is developed that might mitigate the effects jellyfish blooms have on U.S. aircraft carrier's propulsion systems. This technology includes combining a sonar detection which provides early, long range detection of objects and linear bubble tubing that releases bubbles to deter jellyfish from entering a nuclear power plant's intakes (Munday 2022). These rising bubbles collect in the jellyfish's body cavity which causes them to move upward in the water column away from the intake (Munday 2022). This technology could be worth considering if jellyfish become more problematic to U.S. naval operations, regardless of location.

Future work would include development of a TDA which would ingest areas of already active blooms and predict areas of a future bloom based on the available environmental data. This understanding of jellyfish blooms could be expanded to current and future U.S. naval operating areas such as the Mediterranean Sea, Adriatic Sea, and East China Sea. As these areas are not influenced by monsoon seasons, understanding the underlying cause of the various jellyfish blooms might be more related to other types of jellyfish outside of the monsoon region.

LIST OF REFERENCES

Chunlüe, Z., 2023: Empirical Orthogonal Function (EOF) analysis, MATLAB Central File Exchange. https://www.mathworks.com/matlabcentral/fileexchange/54416-empirical-orthogonal-function-eof-analysis.

CMEMS, 2019: Global Ocean Blended Reprocessed Winds. Subset used: 0000 UTC January 1 1993 – 2359 UTC December 2019. Copernicus Marine Service, accessed June 30 2022, https://doi.org/10.48670/moi-00185.

CMEMS, 2018a: Global Ocean Blended Near Real Time Observed Winds. Subset used: 0000 UTC January 1 2020 – 2359 UTC November 15 2021. Copernicus Marine Service, accessed June 30 2022, https://doi.org/10.48670/moi-00305.

CMEMS, 2018b: Global Ocean Biogeochemistry Analysis and Forecast. Subset used: 0000 UTC January 1 2021 – 2359 UTC December 31 2021. Copernicus Marine Service, accessed October 25 2022, https://doi.org/10.48670/moi-00015.

CMEMS, 2018c: Global Ocean Biogeochemistry Hindcast. Subset used: 0000 UTC January 1 1993 – 2359 UTC December 31 2020. Copernicus Marine Service, accessed October 18 2022, https://doi.org/10.48670/moi-00019.

CMEMS, 2016: Global Ocean Physics Analysis and Forecast. Subset used: 0000 UTC January 1 2021 – 2359 UTC December 31 2021. Copernicus Marine Service, accessed June 2 2022, https://doi.org/10.48670/moi-00016.

CMEMS, 2018d: Global Ocean Physics Reanalysis. Subset used: 0000 UTC January 1 1993 – 2359 UTC December 31 2020, Copernicus Marine Service, accessed December 1 2022, https://doi.org/10.48670/moi-00021.

Condon, R. H. and Coauthors, 2013: Recurrent jellyfish blooms are a consequence of global oscillations. *Proceedings of the National Academy of Sciences of the United States,* **110**, 1000–1005.

Daryanabard, R., and Dawson, M. N., 2008: Jellyfish blooms: Crambionella orsini (Scyphozoa: Rhizostomeae) in the Gulf of Oman, Iran, 2002–2003. *Journal of the Marine Biological Association of the United Kingdom*, **88**, 477–483, https://doi.org/10.1017/s0025315408000945.

Dong, Z., Dongyan, L., and Keesing J.K., 2010: Jellyfish blooms in China: Dominant species, causes, and consequences. *Marine Pollution Bulletin,* **60**, 954–963, https://doi.org/10.1016/j.marpolbul.2010.04.022.

Drevillon M., Fernandez E., and Lellouche J./CMEMS: 2018: Product User Manual. Copernicus Marine Service, accessed December 1 2022, https://catalogue.marine.copernicus.eu/documents/PUM/CMEMS-GLO-PUM-001-030.pdf.

Giesen, R., Stoffelen, A., and Verhoef A./CMEMS, 2019: Product User Manual. Copernicus Marine Service, accessed June 30 2022, https://catalogue.marine.copernicus.eu/documents/PUM/CMEMS-WIND-PUM-012-004-006.pdf.

Giesen, R., Stoffelen, A., and Verhoef A./CMEMS, 2018: Product User Manual. Copernicus Marine Service, accessed June 30 2022, https://catalogue.marine.copernicus.eu/documents/PUM/CMEMS-WIND-PUM-012-004-006.pdf.

Google Earth V 9.188.0.0, 2015: Arabian Sea. 15°N 48°W, 15°N 70°W, 30°N 48°W, 30°N 70°W, Eye alt 2950km. SIO, NOAA, U.S. Navy, NGA, GEBCO. Accessed on April 1 2023, https://earth.google.com.

Jayaram, C., Chacko, N., Joseph, K. A., and Balchand, A. N., 2010: Interannual Variability of Upwelling Indices in the Southeastern Arabian Sea: A Satellite Based Study. *Ocean Science Journal,* **45**, 27–40.

Harrison, P. J., Furuya, K., Glibert P. M., Xu, J., Liu, H. B., Yin, K., Lee, J. H. W., Anderson, D. M., Gowen, R., Al-Azri, A. R., and Ho A. Y. T., 2011: Geographical distribution of red and green Noctiluca scintillans. *Chinese Journal of Oceanology and Limnology,* **29,** 801–831, https://doi.org/10.1007/s00343-011-0510-z.

Kennedy, F. and Wilson, S. (2003). *Crambionella Orsini*. *Jellyfish Feature*. photograph, University of California, Merced. Accessed April 5 2023, https://thescyphozoan.ucmerced.edu/Org/JotQ/JotQ_03Apr.html.

Khan, S., Piao, S., Zheng, G., Khan, I. U., Bradley, D., Khan, S., and Song, Y., 2021: Sea Surface Temperature Variability over the Tropical Indian Ocean during ENSO and IOD Events in 2016 and 2017. *Atmosphere*. **12**, https://doi.org/10.3390/atmos12050587.

Lamb, J./JSTOR Daily, 2017: The Global Jellyfish Crisis in Perspective. Accessed February 8 2023, https://daily.jstor.org/global-jellyfish-crisis-perspective/.

Lamouroux, J. and Tonani, M./CMEMS, 2018: Product User Manual. Copernicus Marine Service, accessed October 25 2022, https://catalogue.marine.copernicus.eu/documents/PUM/CMEMS-GLO-PUM-001-028.pdf.

Le Galloudec O., Law Chune S., Nouel L., Fernandez E., Derval C., Tressol M., Dussurget R., Biardeau A., and Tonani M./CMEMS: 2016: Product User Manual. Copernicus Marine Service, accessed June 2 2022, https://catalogue.marine.copernicus.eu/documents/PUM/CMEMS-GLO-PUM-001-024.pdf.

Le Galloudec O., Perruche, C., Derval C., Tressol M., and Dussurget R./CMEMS, 2018: Product User Manual. Copernicus Marine Service, accessed October 18 2022, https://catalogue.marine.copernicus.eu/documents/PUM/CMEMS-GLO-PUM-001-029.pdf.

Mizokami, Y., 2017: China's Aircraft Carriers have a Menance: Jellyfish Swarms. Popular Mechanics, Accessed on February 14 2023, https://www.popularmechanics.com/military/navy-ships/a14017901/china-aircraft-carriers-jellyfish-swarms/.

Munday, E., 2022: Two Unique Technologies Combine to Fight Jellyfish Swarms and Protect Power Plant Intakes, Accessed on May 1 2023, https://www.subsea2020.com/post/two-unique-technologies-combine-to-fight-jellyfish-swarms-and-protect-power-plant-intakes.

NOAA Coastwatch, 2022: ACSPO Global 0.02º Gridded Super-collated SST and Thermal Fronts from Low-Earth-Orbiting Platforms (L3S-LEO), accessed May 15 2023, https://coastwatch.noaa.gov/cwn/products/acspo-global-002o-gridded-super-collated-sst-and-thermal-fronts-low-earth-orbiting.html

NOAA/NCEP, 2010a: Climate Forecasting System Reanalysis Evaporation Duct distributed by National Climatic Data Center. Subset used: January 1993 – December 2010, accessed April 4 2023, https://portal.fnmoc.navy.mil/acaf/.

NOAA/NCEP, 2010b: Climate Forecasting System Reanalysis Ocean Data distributed by National Climatic Data Center. Subset used: January 1993 – December 2010, accessed April 4 2023, https://portal.fnmoc.navy.mil/acaf/.

NOAA/OSMC, 2023a: Dipole Mode Index distributed by NOAA's Earth System Research Laboratories. Subset used: January 1982 – February 2023, accessed April 17 2023, https://stateoftheocean.osmc.noaa.gov/sur/ind/dmi.php.

NOAA/OSMC, 2023b: Niño's 3.4 distributed by NOAA's Earth System Research Laboratories. Subset used: January 1982 – February 2023, accessed April 17 2023, https://stateoftheocean.osmc.noaa.gov/sur/pac/nino34.php.

Pitt, K. A. and Lucas C. H., 2014: *Jellyfish Blooms.* Springer, 304 pp.

Pitt, K. A., Lucas, C. H., Condon, R. H., Duarte, C. M., and Stewart-Koster B., 2018: Claims that Anthropogenic Stressors Facilitate Jellyfish Blooms have been Amplified beyond available Evidence: A Systematic Review. *Frontiers in Marine Sciences,* **5**.

Pourjomeh, F., Shokri, R. S., Rezai, H., Rajabi-Maham, H., and Maghsoudlou, E., 2017: The relationship among environmental variables, jellyfish and non-gelatinous zooplankton: A case study in the north of the Gulf of Oman. *Marine Ecology.* **38**, https://doi.org/10.1111/maec.12476.

Purcell, J. E., Uye, S., and Lo,W., 2007: Anthropogenic causes of jellyfish blooms and their direct consequences for humans: a review. *Marine Ecology Progress Series*, **350**, 153–174, https://doi.org/10.3354/meps07093.

Sanz-Martin, M., Pitt, K., Condon, R., Lucas, C., de Santana, C., and Duarte, C., 2016: Flawed citation practices facilitate the unsubstantiated perception of a global trend toward increased jellyfish blooms. *Global Ecology and Biogeography,* **25**, 1039–1049. https://doi.org/10.1111/geb12474.

Saxena, A. and Menezes, A., 2006: Environmental studies of the Arabian Sea using remote sensing and GIS. *Proc. of SPIE Asia-Pacific Remote Sensing. 2006,* Goa, India, Remote Sensing of the Marine Environment, https://doi.org/10.1117/12.696370.

Shi, W. and Wang M., 2021: A biological Indian Ocean Dipole event in 2019. *Scientific Reports,* **11**, 2452, https://doi.org/10.1038/s41598-021-81410-5.

Soumya, K. R., Riyas, A., Mithun, S., and Biju Kumar, A., 2021, Ethological Studies on the Jellyfish, Crambionella orsini (Vanhöffen, 1888) (Scyphozoa: Catostylidae) in Captivity, *Journal of Aquatic Biology & Fisheries*, **9**, 124–134.

Talley, L., Packard, G., Emery W., and Swift J., 2011: Indian Ocean, *Descriptive Physical Oceanography: An Introduction*, Elsevier, 363–399.

Thomas, L. C., Nandan, S. B., and Padmakumar K.B., 2020, Understanding the dietary relationship between extensive *Noctiluca* bloom outbreaks and Jellyfish swarms along the eastern Arabian Sea (West coast of India), *Indian Journal of Geo Marine Sciences,* **48,** 8, 1389–1394.

Thomson, R. E. and Emery W.J., 2014: The Spatial Analyses of Data Fields. *Data Analysis Methods in Physical Oceanography: Second and Revised Edition*, Elsevier Science, 313–424.

United States Census Bureau, 2011: World Population: 1950–2050, Accessed on February 14 2023, https://www.census.gov/library/visualizations/2011/demo/world-population--1950-2050.html.

Wiggert, J.D., Hood, R. R., Banse, K., and Kindle, J. C., 2005: Monsoon driven biogeochemical processes in the Arabian Sea. *Progress in Oceanography.* **65**, 176–213, https://doi.org/10.1016/p.ocean.2005.03.008.

World Register of Marine Species, 1997: Crambionella orsini, Accessed on 23 April 2023, https://www.marinespecies.org/aphia.php?p=taxdetails&id=220493.

THIS PAGE INTENTIONALLY LEFT BLANK

INITIAL DISTRIBUTION LIST

1. Defense Technical Information Center
   Ft. Belvoir, Virginia

2. Dudley Knox Library
   Naval Postgraduate School
   Monterey, California